Sources of Variability in pre-Bötzinger Complex Rhythmic Patterns Generated by a Transverse Slice

A Thesis
Presented to
The Academic Faculty

by

William C. Gerken

In Partial Fulfillment
of the Requirements for the Degree
Master of Science

School of Electrical and Computer Engineering
Georgia Institute of Technology
April 2003

Sources of Variability in pre-Bötzinger Complex Rhythmic Patterns Generated by a Transverse Slice

Approved by:

Professor Doug Williams, Committee Chair

Professor Robert Butera, Advisor

Professor Robert Lee

Date Approved

TABLE OF CONTENTS

LIST OF TABLES

LIST OF FIGURES

SUMMARY

The pre-Bötzinger complex region of the ventrolateral medulla is a key component of the neural circuitry that generates the respiratory rhythm in mammals. This sub-circuit can be isolated in a slice of brain tissue and within this tissue rhythmicity persists. Our goal in this study is to: 1) characterize the cycle-to-cycle variability of this rhythm; and, 2) utilize a model-based inquiry into the nature of this variability. Such cycle-to-cycle variability is currently not accounted for in existing computational models.

CHAPTER I

INTRODUCTION

1.1 Respiratory rhythmogensis

In order to maintain health and well being in a changing environment, neural control systems are necessarily complex. Understanding how these systems operate is a major topic in neuroscience. One such complex system is respiration in mammals, which requires the uptake of oxygen and release of carbon dioxide by the rhythmic contraction of the diaphragm, intercostal and abdominal muscles. This system must provide for the proper timing of muscle activation, although sensory inputs can modulate respiratory rhythm and pattern [1]. In the neural control system for breathing in mammals, the respiratory rhythm originates in the brainstem [14] from an area called the pre-Bötzinger complex, a bilaterally distributed subregion of the ventrolateral medulla [30, 39]. This discovery led to the development of rhythmic in vitro medullary slice preparations from neonatal and juvenile rodents [16, 29, 40]. In vitro [16, 22, 29, 30, 39] and in vivo [21, 28, 37] preparations have indicated that the pre-Bötzinger complex is necessary and sufficient for generating the inspiratory phase of the respiratory rhythm. It is thought that this region contains the fundamental kernel for respiratory rhythm generation since the rhythm persists in reduced preparations.

The transverse slice generates a stable rhythmic discharge of activity that can be recorded from both the individual cells in the pre-Bötzinger complex and XII motorneurons as well as the ventral roots (Figure 1) [39]. Thin rhythmic slices (200-350 μm) contain the pre-Bötzinger complex and a local network that conveys this rhythmic discharge to the hypoglossal motorneurons [22, 39]. These in vitro preparations of neonatal rat brainstem provide for the study of cellular and network mechanisms of respiratory rhythm and pattern generation in mammals via whole-cell patch clamp recording techniques. The prevailing view suggests the rhythm originates in the pre-Bötzinger complex and is then carried to the XII nucleus by excitatory synaptic transmission [16, 22].

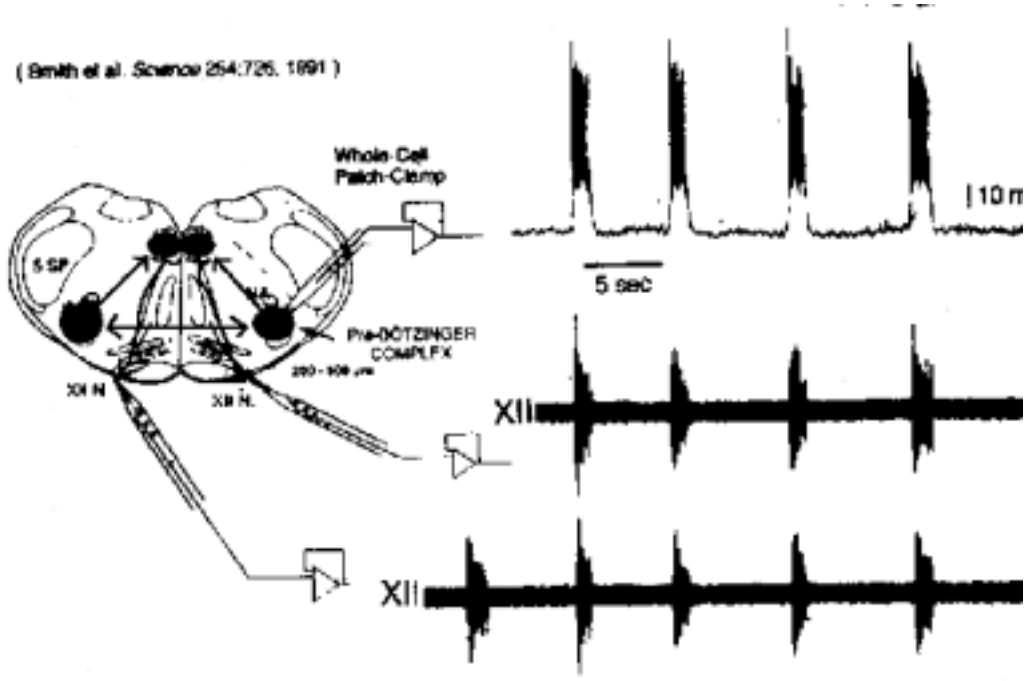

Figure 1: Transverse slice of the brainstem containing the pre-Bötzinger complex and XII nucleus showing concurrent recording via patch clamp on single cell in pre-Bötzinger complex and ventral root

Evidence suggests that rhythm generation in these slice preparations [22, 39] arises from a population of excitatory interneurons with intrinsic oscillatory bursting or pacemaker-like properties. Pacemaker neurons exist in the transverse slice [39] and their activity continues even when synaptic coupling is blocked [20]. Excitatory coupling synchronizes the pacemaker neurons to generate the rhythmic behavior in the pre-Bötzinger complex [22]. This suggests that intrinsically bursting neurons along with the interaction of synaptic properties lead to the generation of the respiratory rhythm [29, 30, 38, 40].

The neural circuitry and electrical properties of both single neurons and the transverse slice have been characterized [9, 10, 20, 22, 39]. The respiratory rhythm is much more complex than a simple sine wave and produces considerable variability even in a reduced preparation such as the transverse slice. However, the fundamental mechanisms of respiratory rhythm generation are still an unsolved problem.

1.2 Computational Modeling

Researchers build conceptual models to try to understand the basic mechanisms underlying a particular process or phenomenon. While it is necessary to abstract away some detail to try to extract the fundamental components of the mechanisms being studied, the conceptual model loses faithfulness to the real process being studied. Often deterministic models are used when modeling a large number of stochastic events. While the deterministic model aids in the comprehensibility of the system, it inevitably leaves out complex phenomenon associated with the stochastic process. The result is a unavoidable trade-off between model complexity/fidelity and comprehension of the model and ideally, the underlying process.

Early network models of respiratory rhythmogenesis have been based on relatively simple models of single neurons and depended on network mechanisms, neglecting the possible role of intrinsic neuronal properties. Subsequent intracellular data combined with advances in computational modeling allowed the development of more realistic and predictive respiratory neurons and, therefore, more faithful respiratory networks. Later computational models of respiratory rhythm [34, 35] are based on either a two (inspiratory, expiratory) or three (inspiratory, post-inspiratory, expiratory) phased network based rhythm. This assumption postulates that the during each phase a subset of neurons fires and inhibits the other neurons in the network. These models rely on inhibitory synapses among distinct populations of neurons for rhythm generation, and much experimental evidence supports these models [1]. However, when synaptic inhibition is blocked in vivo, the respiratory rhythm still persists [14, 17]. Furthermore, these models do not account for the role that pacemaker neurons play in rhythm generation. The hybrid-pacemaker network hypothesis accounts for these deficiencies by proposing a model in which a rhythm-generating population of inspiratory neurons is embedded within a complex pattern forming network [38]. In order to investigate the dynamic interaction between cellular and synaptic properties, models with neuronal ionic conductance mechanisms have been introduced [36]. There are also more parsimonious models that incorporate the critical population of pre-Bötzinger complex pacemaker neurons [3]. This latter model focuses on the minimal ionic currents necessary to generate voltage-controlled bursting and remain consistent dynamic features of experimental

recordings. Additionally, these models account for a wide range of experimental findings such as control of voltage control of oscillatory mode, voltage control of burst frequency, voltage dependent activity modes, and flat baseline membrane potential during interburst intervals. Models are robust over a wide parameter range. It has been shown that large heterogenous networks of these models [4] contain neurons with slow adaptation properties in combination with excitatory synaptic coupling ,which is critical for rhythm generation in the reduced network. This is consistent with experimental findings in the thin transverse slice preparation. If the synaptic connectivity is sufficiently strong, networks of this type are capable of generating synchronous bursting even when none of the neurons are intrinsically bursting. This network model exhibits frequency control of the slice rhythm by membrane depolarization. Decrease in amplitude of the population activity occurs with increased frequency of bursting in the network. Additionally, the effect of synaptic coupling on burst duration of the pacemaker neurons was consistent with the transverse slice data [9].

Since the pre-Bötzinger complex is bilaterally distributed, experimentalists have bisected the slice to determine the effect on respiratory frequency and regularity of rhythmic output [9]. These results confirmed the computational model's prediction [4] of an increase in frequency and decrease in regularity of the rhythm as a result of reducing coupling strength by splitting the slice.

Researchers have explored the dynamics of excitatory networks of bursting pacemaker neurons with heterogeneous properties. While bursting frequency and synchrony can be controlled in such computational models, a set of parameters or conditions have not been formulated that can recreate the rhythmic variability observed in the temporal character of the synchronous burst of the population that occurs every cycle. These deterministic computational models while easy to understand tend to produce very regular bursting. Additionally, while one can qualitatively observe cycle-to-cycle burst variation, a quantitative metric for measuring this rhythmic variability is necessary into order to compare the models to experimental data.

1.3 Quantifying Periodicity and Regularity

While it is quite obvious to the human eye that rhythmic experimental data has a certain amount of periodicity from cycle-to-cycle, conventional signal processing techniques may not be capable of quantifying it in a meaningful way. This is particularly true of bursting systems, which consist of an alternation between a high frequency burst of spikes and a period of silence. Attempts to quantify the bursting nature of the neurons using a frequency-based Fourier approach work well to identify the major frequency components of the signal [33], but may have trouble identifying the periodic oscillations or the degree of consistency of the bursting. This is because this frequency of alternation between the spiking, which makes up a burst, and the silence in between bursts is a low amplitude signal, and this low frequency is very close to DC and can be lost in the noise. One must note that even though time and frequency domain methods both contain the same information about the processes involved, it does not necessarily follow that these representations are equivalent to the observer. Often, striking differences between the appearance of the two different representations of the same data illustrate that mathematical equivalence does not always lead to equivalent emphasis of distinctive features of the data [33].

Work has been done on classifying consistency and signal strength of respiratory neuronal activity [27]. This approach uses a characteristic η^2 to define the amount of the respiratory component in the activity of a respiratory cell, where $\eta^2 = \frac{\sigma_m^2}{\sigma_t^2} = \frac{\sigma_m^2}{\sigma_m^2+\sigma^2}$ and σ_t^2 is the total variance of neuronal activity, σ_m^2 is variance of means across fractions of the respiratory cycle, and σ^2 is the variance within fractions of the respiratory cycle. The index is the proportion of total variance of the activity of a respiratory neuron consisting of the variance occurring across fractions of the respiratory cycle. η^2 values partially depend on the consistency of discharge pattern from breath to breath and partially on strength of the respiratory activity. It was hypothesized [27] that the size of the respiratory component in the activity of different respiratory cells differed among cells but was a stable characteristic of any given cell. While this index classifies cells as being respiratory if the timing of its activity consistently coincides with some phase of the respiratory cycle, very different rhythms can produce the same statistic [27]. Cells that were clearly respiratory because

they consistently discharged at a particular phase in the respiratory cycle, but had a high degree of cycle-to-cycle variability scored the same η^2 as cells that were modulated rather weakly during the respiratory cycle. This statistic also does not quantify overall population rhythmic variability per se, instead it measures individual cells variability versus the respiratory cycle.

While bursting behavior is easily recognizable to the seasoned experimentalist and often times even to the untrained eye, characteristics of bursting signals make them problematic to study with conventional signal processing techniques. Neither a prior single metric, nor a straightforward combination provides an easily intelligible and readily understandable measure of the degree to which the bursting activity of a signal changes temporally.

1.4 Sources of noise and rhythmic variability

1.4.1 Noisiness of ion-channels (switching effects)

The biophysical components of neurons (including synapses and a variety of ion channels) are inherently unreliable and probabilistic [19, 24, 25, 41]. In most models including those cited in this paper, whole cell currents are expressed in terms of a Hodgkin-Huxley formalism that describes the fraction of ion channels in a conductive state. In real life, individual ion channels turn on and off probabilistically and the continuous approximation of a gating variable is not valid at low channel densities. The stochastic Markov version of the Hodgkin-Huxley model converges to the deterministic model as the number of channels becomes large, but in some biologically relevant cases where the number of channels is small, the stochastic model can exhibit behaviors such as spontaneous spiking, bursting and chaos that cannot be observed in deterministic models [8, 42]. The process of spike encoding is therefore noisy and generates variation in the timing of individual action potentials in response to identical inputs [24].

1.4.2 Connectivity patterns

Another proposed source of variability is the effect of connectivity within the network on the network rhythm. While the actual connectivity pattern and range of coupling strengths is still an area of active research, quantitative estimates have been made for the strength

of chemical and electrotonic synapses in the neonatal mouse pre-Bötzinger complex [31]. Bidirectional electrical coupling and unidirectional excitatory chemical transmission are present in the pre-Bötzinger and may be important for the generation or modulation of respiratory rhythm. Computer simulations of populations ranging from fifty to five hundred bursting neurons display coupling effects similar to those found in experimental in vitro preparations [4]. Coupling increases the mean burst duration and decreases the mean burst frequency. Desychronization of the network occurred under conditions of weak coupling, extreme parameter heterogeneity and low-levels of depolarizing background input, gaving rise to a quasi-periodic state. However, the introduction of sparse coupling did not cause desychronization, although it did cause interburst intervals to become more irregular from cycle-to-cycle. Synchrony occurs in networks with probabilistic connectivity as low as 3% [4].

1.4.3 External drive from other populations

It is postulated that the pre-Bötzinger complex receives both excitatory and inhibitory input from populations of tonically firing cells [16, 38, 40]. Non-N-methyl-D-asparate (non-NMDA) glutamatergeric receptors mediate the excitatory synaptic input from the tonically firing population. These beating neurons have been found to provide input with a mean frequency of 10 Hz in vitro [20]. Noisy background input has been shown to enhance the range of coupling strengths where bursting is observed in a population [6]. This situation occurs when the coupling strength is weak. This phenomenon is also observed in individual cells [5] provided the amplitude of the noise is not too large. Asychronous tonic input has been shown [4] to increase the number of cells that burst when uncoupled when compared to the same level of mean-level tonic input. Excitatory background synaptic input can also decrease the burst period of the population.

1.4.4 Oscillators with non-uniform parameters

Real neurons possess considerable variability in their intrinsic membrane parameters, such as maximal conductance. This variability is unaccounted for in determinstic models. This can limit the ability of a determinstic model to account for behaviors exhibited in the real

system. For example, while individual cells may not possess the narrow parameter regime required for bursting, in a strongly coupled population, cells with too much of some current can be balanced by cells that have too little [6]. This offsetting behavior increases the likelihood that the entire group can achieve synchronous bursting.

1.5 Summary

We introduce a novel metric for characterizing rhythmic variability. A bursting neuron model has been developed and implemented in a network setting that will allow us to model the transverse slice containing the pre-Bötzinger complex. We will then study how incorporating proposed mechanisms for creating rhythmic variability into these models alters the rhythm in the simulations. Then, we will use our metric to characterize experimental data and compare these results with those obtained from the simulations. A model is presented for increasing the computational performance of the simulations. Finally, findings of the study are summarized and future directions of the project are discussed.

CHAPTER II

DEVELOPMENT OF RHYTHMIC PERIODICITY METRIC

2.1 Motivation

One goal of the proposed research is to develop a metric for characterizing cycle-to-cycle variability in burst duration and burst interval (i.e. quantifying consistency and strength of bursting in a data set). The developed method should be robust in the presence of noise. This method should also work with all types of bursting data, such as a population recording or an extracellular recording from a single neuron. The underlying assumption is that bursting data has a temporal regularity. One can see a varying degree of this temporal regularity in raw data recordings among the different concentrations of extracellular K^+ concentration (Figure 2). A metric should quantify this regularity by identifying when the burst begins and terminates and quantify the variability of this periodicity.

2.2 Previous approaches

An initial approach was to use a frequency domain technique. This provided a quantitative indication of the frequency content of the signal. The Fast Fourier transform (FFT) is the most widely used method for obtaining the spectral parameters of a neurological signal [26]. The FFT is computationally simple and fast. However, power in the larger peaks of the spectrum tends to leak into a neighboring peak with lower power, because any finite signal has an implicit window around the signal. In the frequency domain, this is equivalent to convolving the spectrum of the signal with the spectrum of the rectangular "window". The frequency spectrum is broadened by incomplete bursting cycles at the end of the signal. The resulting leakage distorts the actual shape of the signal's spectrum both in amplitude and frequency. This is particular alarming if you are trying to measure variability in periodicity, because one possible metric would be the width of the peak corresponding to the burst

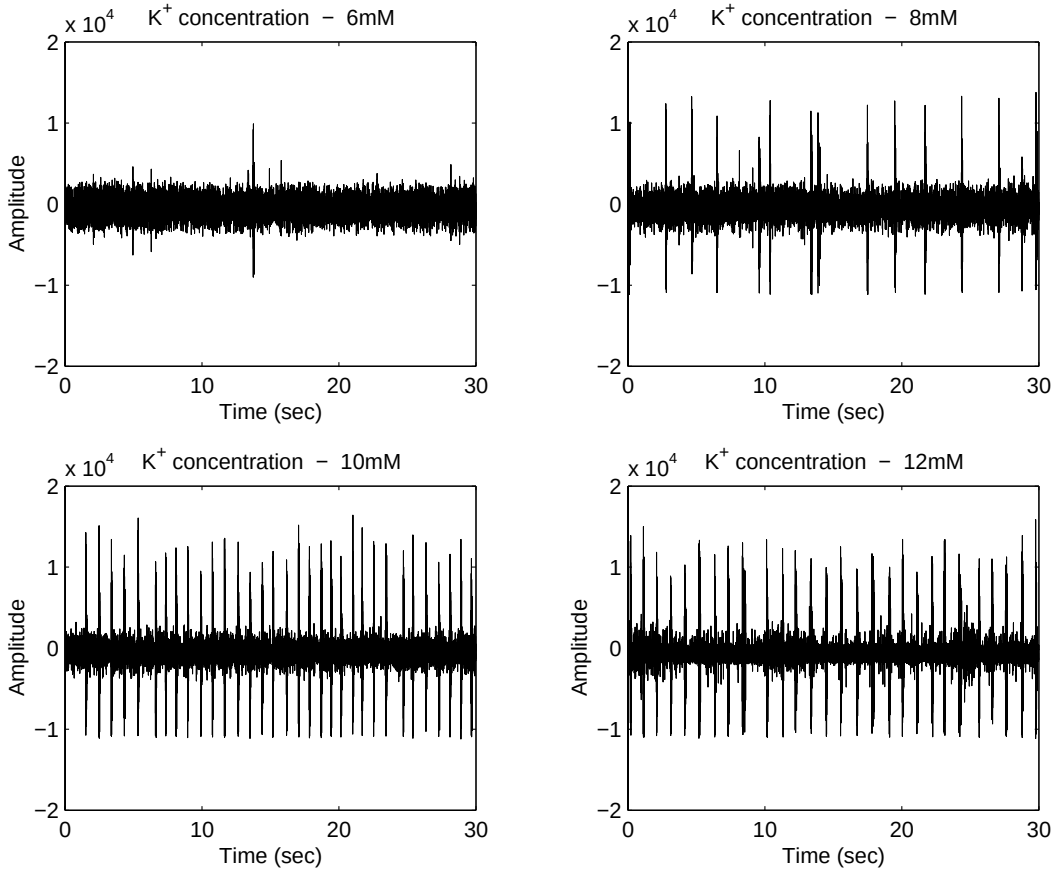

Figure 2: Raw A/D data sampled at 4000 Hz and low-pass filtered at 1000 Hz from UCLA data set at varied extracellular K^+ concentrations (A) 6 mM (B) 8 mM (C) 10 mM (D) 12 mM

period. Due to this spectral leakage, it would be hard to make this system robust across varied data sets. Windowing the signal using a window such as hamming, Chebyshev, or triangular before performing the FFT will reduce leakage effects, which are proportional to the maximum of the window function kernel. This would corrupt any overall measure of variability based on each window. Even so, this leads to a series of spectral content over time and does not summarize the varibility in a straightforward manner. Single spurious events can seriously distort the spectrum content in a single window. Still, this leakage is most disruptive when trying to detect small signals in the presence of large signals, as is the case with bursting. A second issue with the FFT is dependence of resolution on the length of the time series data. Resolution is the measure of the ability of an algorithm to distinguish between two distinct peaks in the spectrum [26]. This severely limits the minimum size

of signals that can be processed with a given degree of resolution of spectral components. Ideally, the most dominant signal would correspond to the burst period. Because the frequency corresponding to bursting has a very low amplitude and is very close to the DC component, the main bursting frequency is often hard to precisely detect in the presence of noise (Figure 3). The high frequency spiking component also tends to dominant the FFT of bursting signals. There is no straightforward way to determine the burst duration from these measures. Furthermore, these frequencies do not directly show changes in variability from cycle-to-cycle though they can be inferred by the width of the peak.

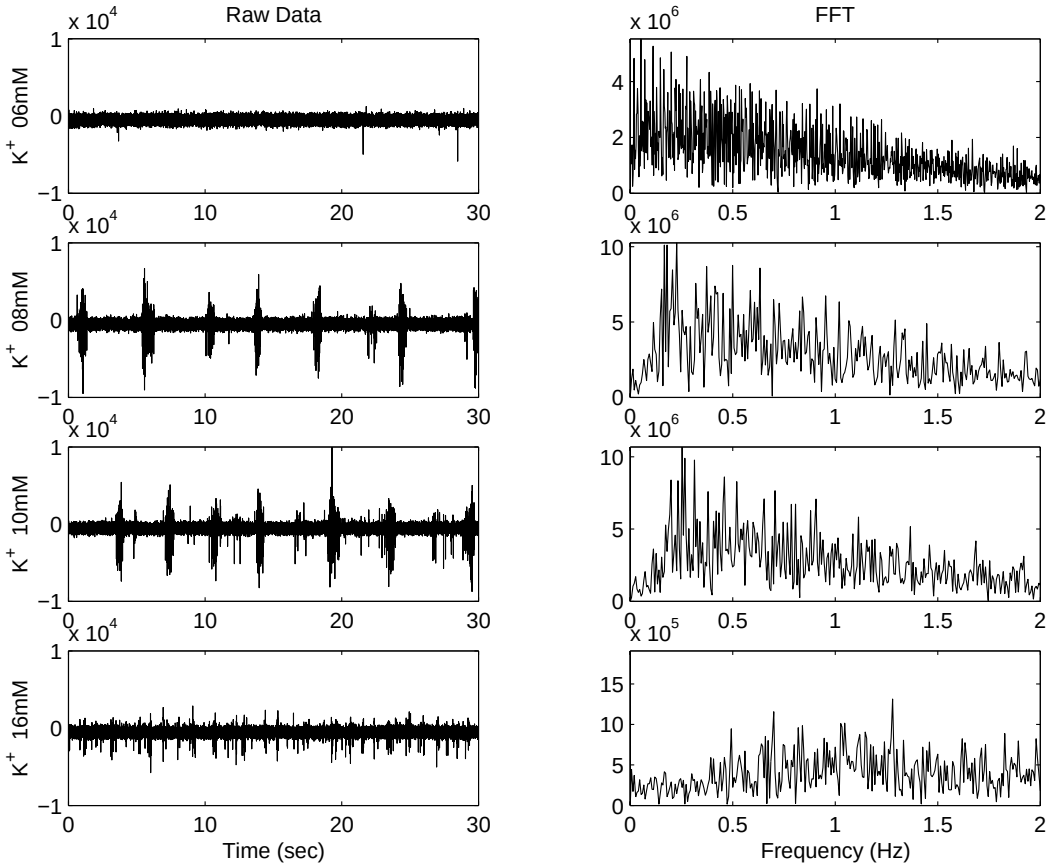

Figure 3: Fast Fourier Transform of NIH data at varying extracellular K^+ concentrations

Time-frequency representations are gaining popularity in signal classification. These techniques can reveal changes in the spectral content over time. Examples of these techniques include the short time Fourier transform (STFT), Wavelet transform, and Wigner-Ville distributions [26]. The wavelet transform uses short windows at high frequencies and

long windows at low frequencies. This transform is able to provide arbitrarily good frequency resolution at low frequency and arbitrarily good time resolution at high frequency [26]. This works well for signals composed of high frequency components of short duration and low frequency components of long durations, as one might expect a bursting signal to be. When one uses a Haar wavelet to decompose a large time-series of bursting data (Figure 4), one discovers the quite intuitive result that high frequency components increase during the population burst. However, there is a similar issue to the FFT in that while one can visually compare the frequency content of each burst to a subsequent burst and try to quantify variability, this approach fails to provide a natural singular measure of the degree of variability.

Traditional frequency domain techiques fail to adaquately characterize the bursting nature of signals, due to the intrinsic characteristics of the signal. Low frequency burst alternating is often lost in the noise. Even if the low frequency component can be found, characterizing variability by inferrence from the size of the spectral peak is far from straightforward. Time-frequency methods can better represent the change of spectral content and thus variability over time, but lack a defining singular metric.

2.3 A Straightforward Novel Approach

Due to the shortcomings of existing approaches, it was determined that a new approach was needed that could fully characterize the periodicity of bursting data in a compact form. We will introduce burst period (BP) and coefficient of variance of burst period (CV) as the two measures of rhythmic periodicity.

2.3.1 Preprocessing

The XII ventral root patch-clamp recording was collected as a raw integer from a A/D board. Experimental data was collected at 4000 Hz and low-pass filtered at 1000 Hz, thus no aliasing. Then the low-pass filtered data is AC-rectified in order to show overall level of activity regardless of polarity. The mean is then subtracted to eliminate any DC offset. Thus, each point represent a temporal sum of local activity. Since the ventral root has the effect of summating the local population activity in the pre-Bötzinger, individual computer

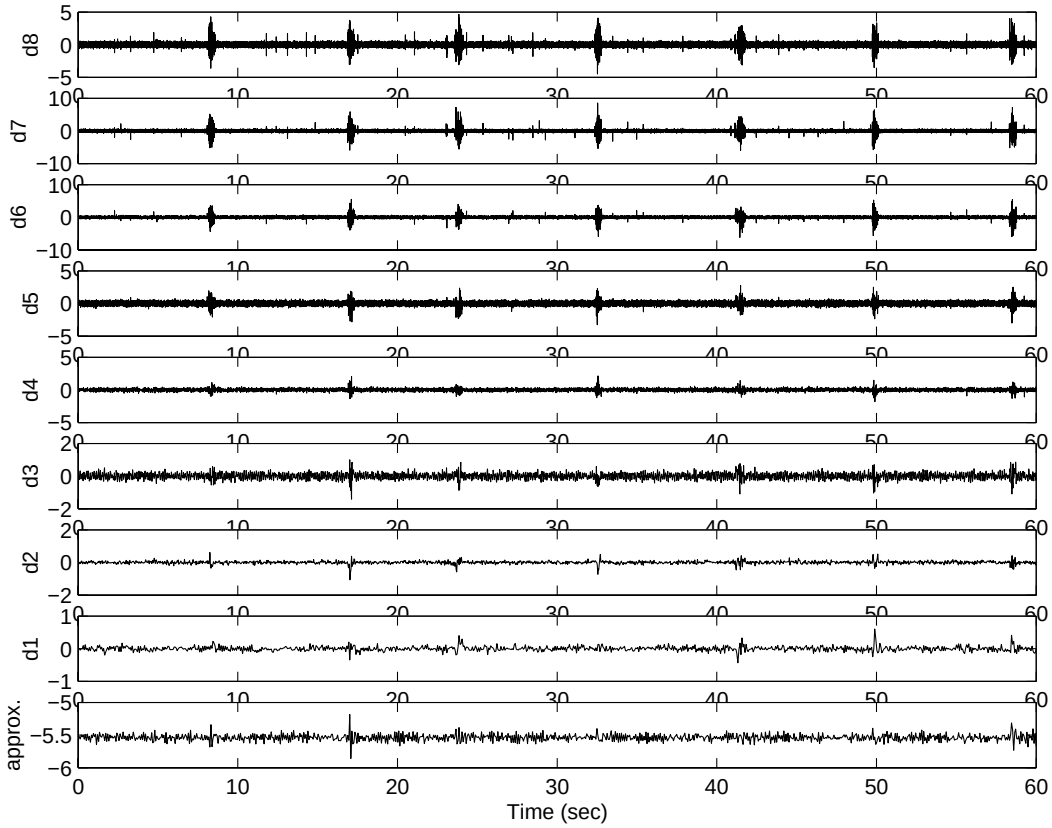

Figure 4: Haar Wavelet decomposition of NIH raw data (control data)

model cells were summated into 10 ms bins to produce a population level signal equivalent to the ventral root output.

2.3.2 Definition of analysis parameters

The data is first windowed to capture the spiking activities of many concurrent neurons while smoothing away single outliers (Figure 5). Most values of window size above 10 ms effectively smooth away ectopic spikes, while too large of a window size tends to artificially lengthen the burst duration, and sets an upper limit on the frequency of the activity that can be represented since it is essentially a low-pass filter. However, since we are interested in the variance of burst period the physiological range of burst period allows a degree of freedom in setting window size, since the upper constraint is $\sim$ .9 Hz which corresponse to a minimum window size of over 10,000 ms. The windowing process effectively creates an envelope around the burst, which is shown as the burst envelope in Figures 5, 6 & 7.

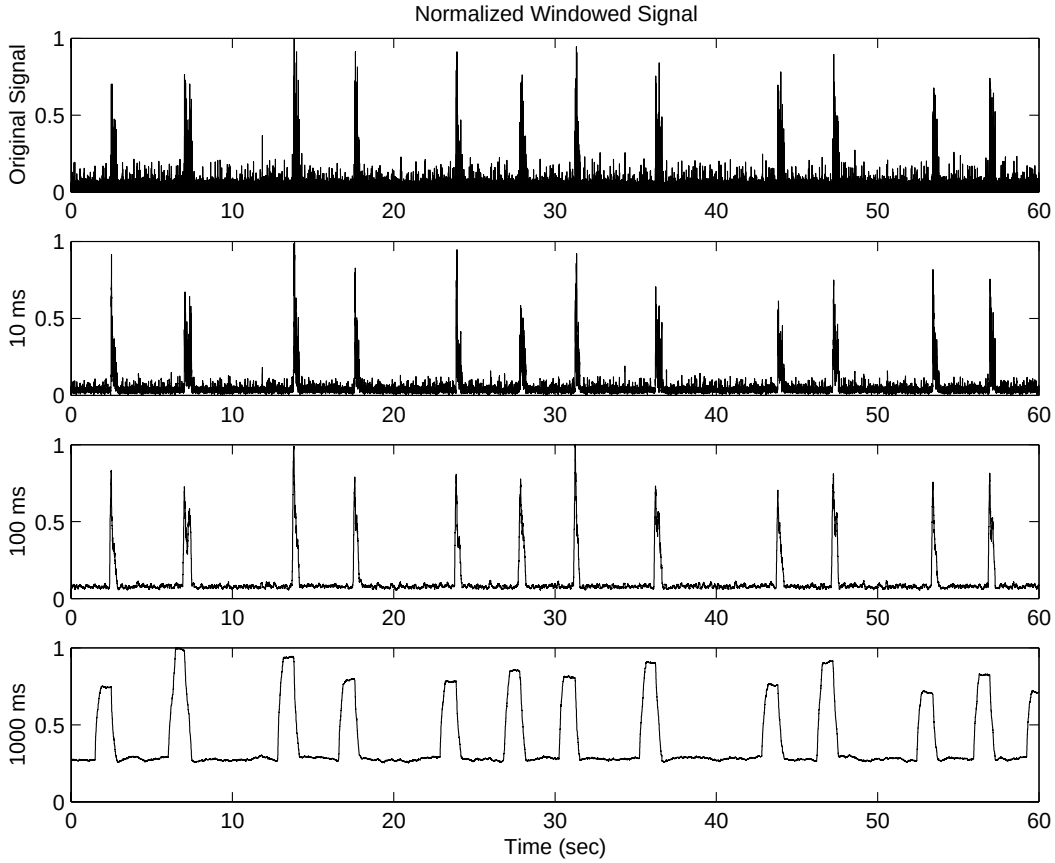

Figure 5: Demonstration of the effects of convolution window size on AC-rectified NIH data

A threshold level is set as a percentage of the dynamic range (i.e. the difference between maximum and minimum values) of the windowed data and is also shown in Figure 6. Samples in the burst envelope above this threshold will be considered to be representing bursts. As one can see in the windowed data (Figure 5), a wide range of threshold values would produce very similar results because the bursts clearly differentiate themselves from the epiotic spikes during the silent periods. Different threshold levels may shift the start and end of a burst but such a shift would be on a much smaller time scale than burst period and would affect all bursts to a similar but often not identical degree. The threshold setting is also sensitivity to fluctuations of the signal amplitude over time. If the slice starts to output increasingly stronger bursts of greater amplitude earlier bursts may not be recognized if threshold is set relatively high. Conversely, a low threshold will pick out spurious bursts if the signal is very noisy. Fortunately, it is shown to be robust (Figure 8).

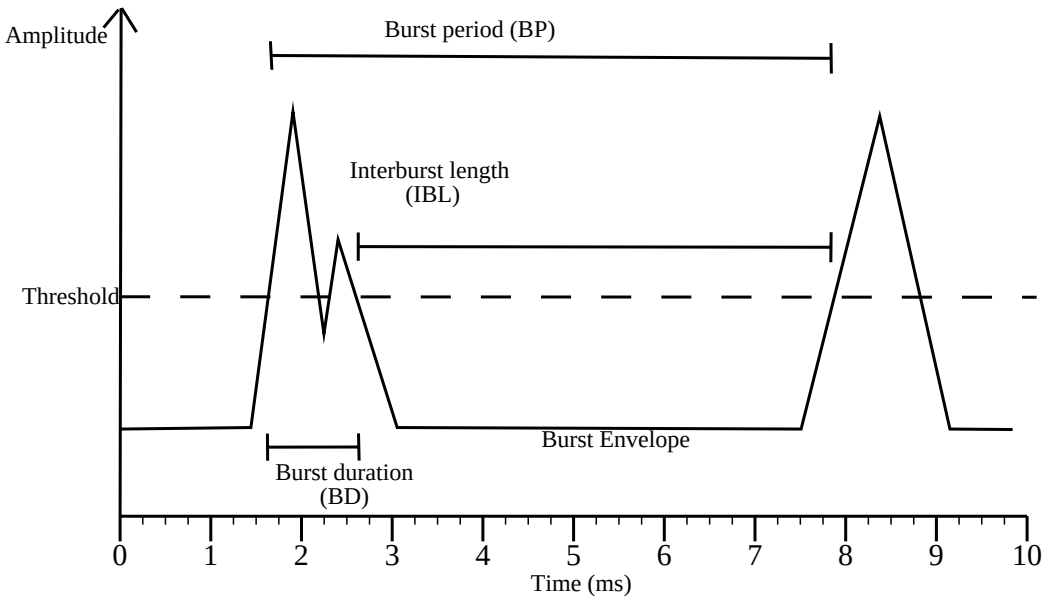

Figure 6: Idealized representation of characterization algorithm

Even if the burst envelope falls below the threshold, if the burst envelope again rises above threshold within the minimum interburst interval it will be considered part of the same burst. The minimum interburst interval has effect of determining how closely bursts can occurs and still be considered separate events. Note in Figure 6 that though the enveloped burst drops below the threshold at 2.25 ms, this does not terminate the burst because the signal rises before the elapse of the minimum IBL. An overly high setting of minimum IBL all activity will be considered as part of a single burst. The disadvantage of low settings of IBL is the potential to divide up a single burst into multiple parts and thus vastly distort both the CV and burst period calculations. Fortunately, CV and BP is shown to be extremely robust across a wide range of IBL (Figure 8).

To summarize in terms of physiological events, the window size acts as a filter on the minimum number of spikes in a fixed time period that will be considered a burst; the threshold acts as a trigger on amount of activity needed to start and end a burst; and the minimum IBL sets a minimum resolution size on how close bursts can be together.

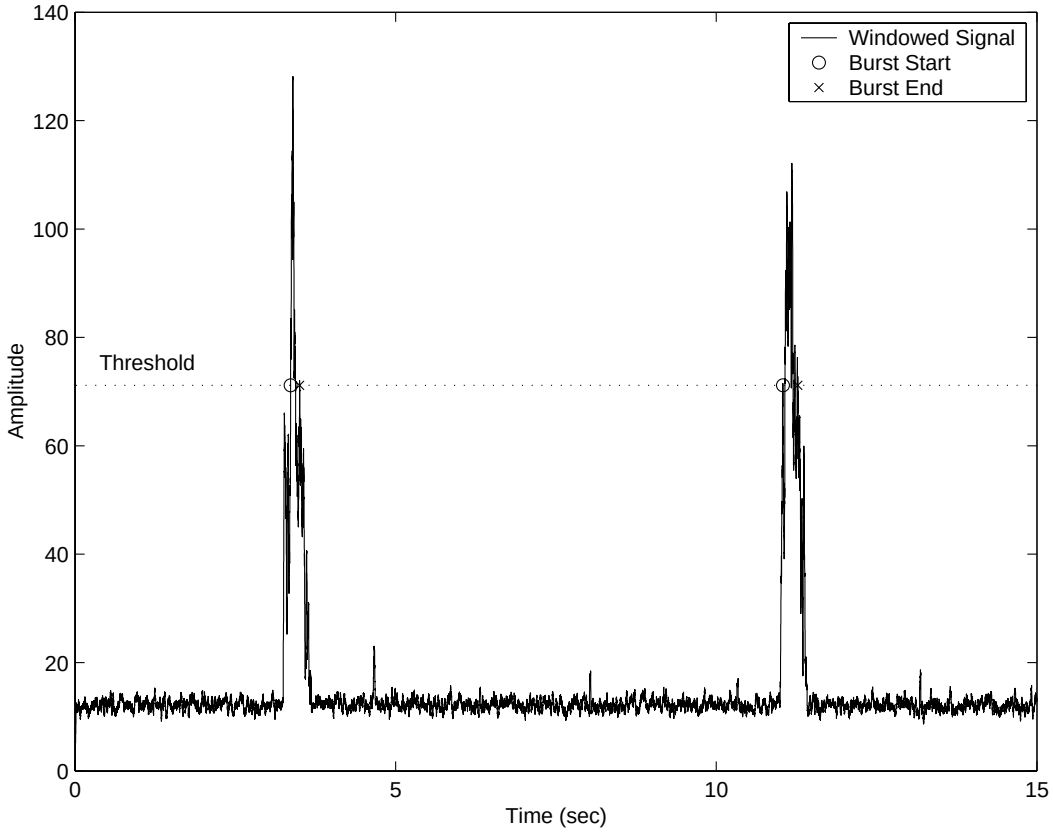

Figure 7: Actual Data manipulation by characterization algorithm

2.3.3 Determination of parameters

To determine the setting of the characterizing parameters, an analysis was performed varying the three parameters. Window size proved to be the most robust and thus was fixed while varying the threshold and minimum interburst interval (Figure 8) in order to determine the parameter sets that minimized the coefficient of variance (CV) for a particular data set. We used a long "clean" data set in which bursts appeared clearly distinct from periods of silence to the eye. This is an acceptable methology since this visual parsing of the bursting behavior is what we are trying to quantify. The parameters were swept over a wide range of physiological or theoretically relevant values. Window size ranged from 10 to 1000 ms until settling on 20 ms into to fix the calculation of characterization for the other parameters. Minimum IBL was swept from 50 ms, which allows resolution up to 20 Hz, to 5 seconds, and likewise threshold was swept from 10-100% since very small values would classify the entire signal as a single burst. This analysis was done because we are using

this metric to emphasize periodicity and regularity. A minimal CV parameter set should be the one that most aptly captures the periodic nature of the signal. That is since our eyes see very little variability in this data set, we should select parameters that produce a metric that indicates very little variability. Fortunately, window size and minimum IBL are extremely robust over the range of physiologically relevant values. Threshold is robust within non-extreme values (i.e. 30 - 70%). Extreme values of the parameter sets (threshold $> 90\%$ or minimum IBL > 10 sec for a highly active slice) give predictable faulty results.

Though not used as to characterize variability, the burst duration can be calculated by measuring the amount of time between the crossing of the threshold ("x" in Figure 7) and the start of a "quiet" interburst interval (IBL) ("o" in Figure 7) of some minimum size. The end of a burst is defined as the last point in time where the window exceeds the threshold preceding an interval of at least the minimum interburst interval. Only completed bursts, that is a burst start and subsequent burst end within a data set are used to calculate burst duration. Similarly, the burst period can be calculated by finding the time between the start of each burst. The mean as well as the coefficient of variance of both burst period and burst duration can be calculated then for the set of bursts contained in each data set.

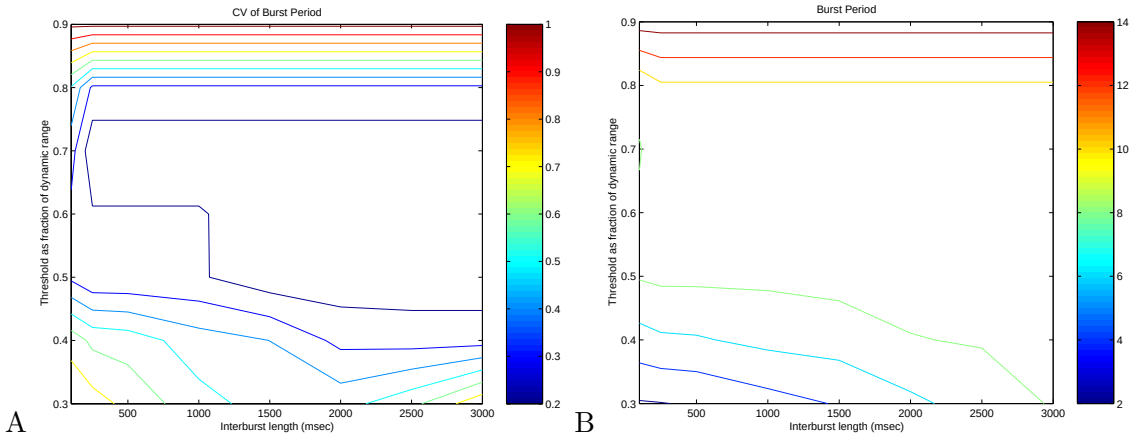

Figure 8: Characterization results as a function of Dynamic Range Threshold and Minimum Interburst length (control data) (A) CV of Burst Period (B) Burst Period

Based on the global minima in Figure 8, the parameters were selected that minimize CV. We chose a parameter set with a window size of 20 ms, minimum interburst interval of 500 ms and threshold of 70% of the dynamic range work. It is important to point out

that we are less concerned about finding an ideal fit for the "clean" data, but instead trying to pick a parameter regime that is very robust while characterizing the low variability that is observed by the eye. Notice that there are a wide range of parameter values that give similar characteristic results indictating robustness. IBL was selected as low as possible while retaining robustness in order to maximize frequency resolution.

2.4 Summary

Since previous methods for classifying rhythmic periodicity were lacking, we have created our own characterizing metric. This metric has three key parameters: window size, which eliminates ectopic spikes in the population; threshold, which ensures that a sufficient amount of activity is occurring; and minimum interburst length, which distinguishes spacing between bursts. By using a sample data set and minimizing CV on it via parameter selection, we have established a parameter set that we will use to characterize all other data. This characterization metric is robust and clearly defines rhythmic variability; therefore, it meets our stated goals.

CHAPTER III

MODEL DEVELOPMENT

A model has been proposed [3, 4] to account for the generation of respiratory rhythm in vitro medullary slice preparations from neonatal and juvenile rodents. In this model, respiratory rhythm is generated by the dynamic interactions of both intrinsic and excitatory synaptic properties within a distributed population of heterogeneous coupled neurons, many of which have bursting pacemaker properties. Since there is currently limited experimental information on ionic and synaptic mechanisms generating and controlling the rhythmic bursting of pre-Bötzinger pacemaker cells, it is reasonable to propose a minimalist model with reduced parameter sets that captures the essence of current experimental measurements and hypothesizes for cellular properties and synaptic interactions. A hybrid pacemaker network has been proposed, which can be modeled by a heterogenious population of these minimalist single cell models coupled by excitatory synaptic connections.

3.1 Methods

All simulations were performed on the CSIP beowulf cluster, which has 1x quad processor server (Xeon 500Mhz) with 1GB of ram, 1x bi-processor Dell PowerEdge 2500 for file server, 16x bi-processor nodes (Pentium III 800Mhz) with 1GB of ram 10x bi-processor nodes (Pentium III 933Mhz) with 1GB of ram and 1x HP Procurve 4000 for the network backbone. All simulations were performed using NEURON version 5.4 [18], a simulation environment for developing and simulating models of neurons and networks of neurons, using the built-in CVODE integrator with error tolerance of 1e-4. Threshold crossing detection and the handling of synaptic events were facilitated by NEURON's event handling features. All signal processing techniques were performed using MATLAB 6.1. The wavelet computations were done using the MATLAB Wavelet Toolbox Version 2.1. The paired sample analysis was performed using the StatPro add-in for Microsoft Excel.

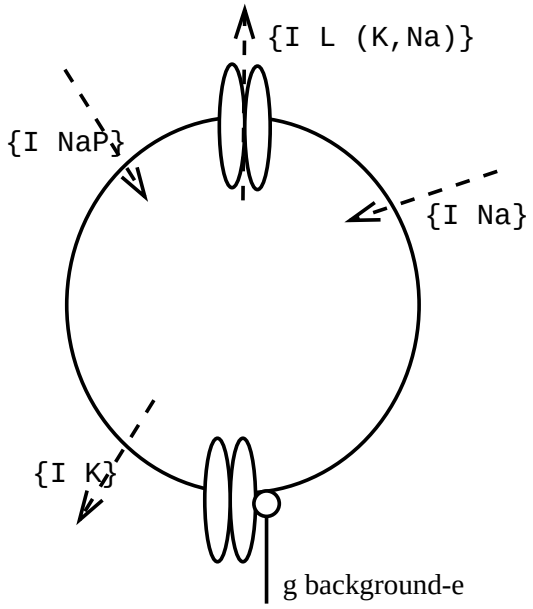

Figure 9: Model burster cell showing intrinsic currents and excitatory background input

3.2 Single cell model

In the single cell model bursting occurs via fast activation and slow inactivation of a Ca^{2+} -independent persistent Na^{+} current. This model displays dynamic features that occur in electrophysiological recordings from the pre-Bötzinger oscillatory bursting neurons in vitro [3]. These features include voltage-dependent activity modes (silence, bursting, and beating), a voltage-dependent burst-frequency that varies from 0.05 to greater than 1 Hz and a decaying spike frequency during bursting. This model is robust and persistent across a wide range of parameter values. Also, this model is consistent with experimental data as burst duration decreases as the baseline membrane potential is depolarized [3]. The model also displays a relatively flat membrane potential trajectory during the interburst interval. This is a single compartment model conceptually modeled as a 13 μm spherical soma. Cell and neuron are used interchangeably throughout this chapter to refer to a single instance of the single compartment model.

This model uses a three-variable Hodgkin and Huxley formulation of respiratory bursting neurons in the pre-Bötzinger complex of mammals [3]. These models use two simplifications from the standard Hodgkin and Huxley model. Since the gating variable m activates on a

much faster time scale compared to the other dynamics, it can be assumed to be instantaneous without significantly changing the dynamics of the model [32]. A second simplifying assumption is the characterizing of the time course of the gating variable h as $1 - n$ [32]. Quantitative measurements of the gating characteristics of I_{Na} and I_K have not been made in respiratory neurons [3].

The model's dynamics are described completely by an autonomous set of differential equations (Equations 1-6).

$$C\frac{dV}{dt} = -I_{Na}(V) - I_{NaP-h}(V) - I_K - I_{L(K)} - I_{L(Na)} + I_{app} - I_{syn} \tag{1}$$

The transmembrane current is calculated by Kirchoff's current law and is the sum of intrinsic and externally applied currents. C is the whole cell capacitance in pF. For all simulations, C is set to 21 pF, which is consistent with whole cell measurements from inspiratory neurons in vitro [39]. I_{app} is added for completeness but not used in any of the simulations.

A fast Na^+ current (I_{Na}) and delayed-rectifier K^+ current (I_K) generate action potentials.

$$I_{Na} = g_{Na}m_\infty^3(V)(1-n)(V - E_{Na}) \tag{2}$$

$$I_K = g_K n^4 (V - E_K) \tag{3}$$

There is also a slow inactivating Na^+ current in which the activation of m_∞ is also considered instantaneous because it is several orders of magnitude faster than the time scale of h. This model also contains a leak current with K^+ and Na^+ components which allows us to simulate changing extracellular K^+ concentration by varying E_K in the model (Figure 9).

$$I_{NaP-h} = g_{NaP-h}m_\infty(V)h(V - E_{Na}) \tag{4}$$

$$I_{L(K)} = g_{L(K)}(V - E_K) \tag{5}$$

$$I_{L(Na)} = g_{L(Na)}(V - E_{Na}) \tag{6}$$

Voltage dependent activation and inactivation variables regulate the conductances of the ionic current. For each gating variable x, the governing dynamics are described by $x_\infty(V)$, the steady-state voltage-dependent (in)activation function of x and $\tau_x(V)$ is the voltage-dependent time constant. $x_\infty(V)$, which is a sigmoid with a half-(in)activation at V = θ_x and a slope proportional to $1/\sigma_x(V)$, which is a bell-shaped curve that has a maximal value $\bar{\tau_x}$ at $V = \theta_x$ and a half-width determined by σ_x. For parameter values, the values for model I [3] are used unless otherwise stated.

$$\frac{dx}{dt} = \frac{x_\infty(V) - x}{\tau_x(V)} \tag{7}$$

$$x_\infty(V) = \frac{1}{1 + exp\frac{V-\Theta_x}{\sigma_x}} \tag{8}$$

$$\tau_x(V) = \frac{\tau_x}{cosh\frac{V-\Theta_x}{2\sigma_x}} \tag{9}$$

In order to implement this model in NEURON, the whole cell conductances must be converted into conductance densities. The geometry of the cell is defined to be a open ended cylinder with length of 26 μm and diameter of 26 μm, which is equivalent to a 13 μm sphere. This required the whole cell conductance (nS) to be multiplied by a factor of 0.047 to convert into densities $\frac{\mu S}{cm^2}$.

3.3 Network model

We created network simulation models in NEURON using a burst capable neuron model [3], in a heterogeneous network [4] coupled by excitatory AMPA synapses. Output from the simulations was captured through a raster recorder. Premilinary studies with spatial and temporal effects were created by restricting cellular connectivity and specifing synaptic delay. However since the transverse slice is relatively small, it is reasonable to assume that all cells are connected with little delay. Therefore, all simulations in this study have all-to-all connectivity and zero temporal delay unless otherwise noted. Whenever a cell's membrane potential crosses a fixed threshold voltage of -10 mV, the cell identification and time is recorded (Figure 10 A). Using this data, a population activity measure can be created by windowing the data and summing the individual neuron spikes (Figure 10 B). Raster

data is considered sufficient since subthreshold fluctations in an individual cell's membrane potential are virtually undetectable in summated population data both in real neurons and in simulation studies.

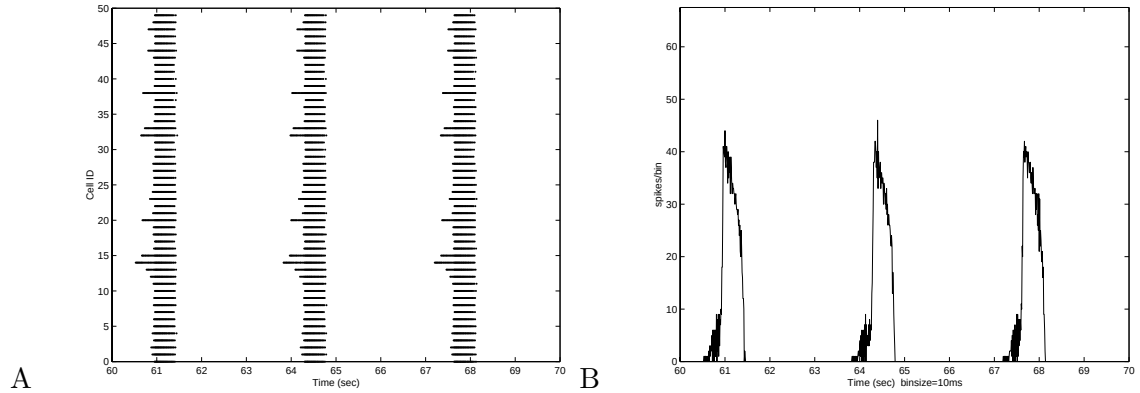

Figure 10: Network simulation (50 burster cells), e_K = -82 mV and Independent Poisson-distributed Background Input) (A) Raster recording (B) Temporally summated 'population' data

A simple model for glutamate AMPA receptors [13] can be used to model both the excitatory synaptic coupling connections within the pre-Bötzinger complex and the excitatory synaptic connections between the the background cells and the pre-Bötzinger complex. The simplified model was obtained from a detailed synaptic model that included the release of transmitter in adjacent terminals, its lateral diffusion and uptake, and its binding on post-synaptic receptors [12]. Short pulses of transmitter with first-order kinetics were found to be the best fast alternative to represent the more detailed models. The first-order model can be solved analytically, since no differential equation must be solved (Equations 10 - 15). This makes this method a very fast mechanism for simulating synapses.

$$R_\infty = \frac{\alpha}{\alpha + \beta} \tag{10}$$

$$R_\tau = \frac{1}{\alpha + \beta} \tag{11}$$

$$R'_{on} = \frac{R_\infty - R_{on}}{R_\tau} \tag{12}$$

$$R'_{off} = -\beta * R_{off} \tag{13}$$

$$g_{syn} = R_{on} + R_{off} \tag{14}$$

Parameter	Value
N (# of cells)	50
p	1
Synaptic delay	0 ms
Synaptic strength	.1 nS
Background input	.3 nS
CVode relative tolerance	1e-4

Table 1: Default parameters values for simulations

$$I_{syn,j} = (\Sigma_{i=1}^{N} \bar{g}_{syn-e,i,j})(V_j - E_{syn-e,j}) \tag{15}$$

The reversal potential for the synapse is 0 mV. The forward binding rate α is .94 ms^{-1} and the backward unbinding rate β is .18 ms^{-1}, which corresponds to a first-order fit on whole-cell kinetics [43].

All pre-Bötzinger complex network simulations are constructed of 50 burster neuron models unless otherwise noted. The burster cells deliver output to other burster cells via AMPA synapses. They can also receive "simulated" excitatory background synaptic input from a population of 100 tonic firing cells. Since we are using a single compartment model for the burster cell, all synapses were set to terminate in the middle of the soma, the lone compartment.

3.4 Proposed mechanisms for creating variability

3.4.1 Ion channel noise

Ion channel effects will not be considered in this study because simulating such processes is computationally intensive, even for a single neuron. Incorporating these effects would vastly expand the scope of this study and drastically decrease computational performance of the network simulations. Additionally, in large networks with sufficient coupling like in this study, the noise is filtered by the effectively shared capacitance and the underlying deterministic dynamics are expressed [7].

3.4.2 Probablistic Connectivity

Network models in this study can be configured using probabilistic or deterministic connectivity. In the case of probabilistic connectivity where the probability of a synaptic connection

existing between any 2 pairs of cells is p, a uniform random number generator was used to determine whether a particular connection existed. A cell is not allowed to connect to itself. To compensation for the loss of synaptic input from "eliminated" synapses, the synaptic strength was scaled by 1/p to maintain similar network dynamics. This ensures that the differences between a fully and sparsely connected model are not simply a result of different levels of total synaptic input to individual cells in the network.

3.4.3 External drive from populations of tonically firing cells

Since pre-Bötzinger cells are postulated to receive low-frequency background input from surrounding cells, the model can also incorporate background excitatory synaptic input. For simplicity we consider only excitatory input although analogous results have been obtained if a mean-level of inhibitory input is considered as well [4]. In this study, this background input is conceptually modeled by a population of cells that give input at a frequency of 10 Hz. In the simulation , this is implemented by one "independent source" and one global source for each cell. The weights of each connection can be manipulated to study the effect of the degree of correlation of background input. The spike rate was then chosen based on an assumption for the number of cells times the spike rate of 10 Hz/cell. This is implemented by setting a uniform fixed spike interval for the independent and global source. Shortening (lengthening) this spike rate interval has the effect of raising (lowering) the mean-level of background input. Also, this could be conceptually thought of as increasing (decreasing) the size of the population, since the number of cells times spike rate equals the total number of spikes received by the slice.

As far as the actual number, there has been no estimate in experimental literature. The patterns in which background input connects to pre-Bötzinger complex neurons are likewise unknown. Instead, we present a noisy summated input generated by tonically firing cells.

The background input is connected independently and individually to each burster cell (Figure 11 B). The starting time of each background input is randomized uniformly between 0-1 ms to ensure that individual inputs are uncorrelated in phase. The background input can also be connected globally, meaning all cells receive the same input from the background

(Figure 11 C). The background cells can output three distinct types of signals: constant-level, periodic spiking and poisson-distributed spiking, as well as weighted combinations of these types (Figure 11 A). The periodic input delivers a spike event at a regular interval without variation, while the poisson-distributed input delivers spike events according to a poisson process. The constant-level input provides a mean-level equivalent to the periodic and poisson-distributed spiking cells. This was done by measuring the conductance at each time step, discarding the first sixty seconds to allow transients to decay and then taking the mean. The periodic spiking input is set to deliever a set amount of synaptic input and then the constant-level input is adjusted to be the same mean-level. The poisson spiking input is created by taking the periodic spiking input and allowing spiking to varying according to a poisson process. Mechanisms have been developed to control the correlation of the individual background inputs, by connecting both the global and individual background inputs and then weighting there respective inputs. In NEURON, the constant-level input was modeled as a conductance density, while the spiking inputs were implemented as point processes. This required that the constant-level needed to be scaled much like the ionic current densities.

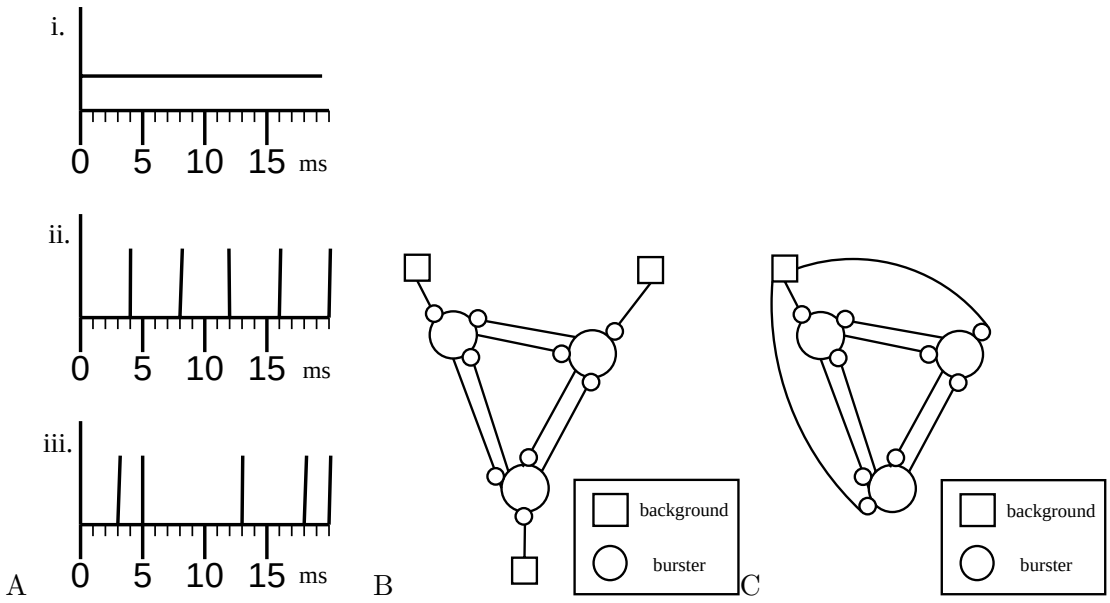

Figure 11: Modeling and configuration of excitatory background input (A) Three forms of input i.) Constant-level ii.) Periodic spiking iii.) Poisson-distributed spiking (B) Individually connected network - three burster cells (C) Globally connected network - three burster cells

Parameter	Mean	Standard Dev.
g_{syn} (n=50,p=1) (nS)	.1	.025
g_{NaP} (nS)	2.8	.4
$g_{L(K)}$ (nS)	.11424	.01142

Table 2: Distribution of Intrinsic and Synaptic Model Parameters

3.4.4 Intrinsic and Synaptic Heterogeneity

In contrast to deterministic model neurons, real neurons have considerable variability in their intrinsic membrane parameters. In order to introduce this variability into the simulation, we chose to make g_{syn} and g_{NaP} heterogeneous throughout all simulations. Additionally, we have made $g_{L(K)}$ in Section 4.1.1 and 4.3 to show effects of heterogeneity of baseline level of depolarization. In Figure 14, we presented the results of consolidating the Na^+ and K^+ leak channels into a single heterogenous leak channel by varying E_L to make comparison to prior work [4]. g_{syn} is the coupling strength between individual neurons. g_{NaP} determines the ability for a cell to intrinsically burst. $g_{L(K)}$ is conductance of the K^+ leak channel [9], which plays a role in determining the baseline level of membrane depolarization. Likewise, E_L determines the baseline level of membrane depolarization in the simulation with a single leak channel. Parameters were chosen from a normal distribution with a specified mean and standard deviation (Table 2). The standard deviations were chosen so that the distributed parameters fell within a range of dynamic behaviors. Previous work [4] has indicated that simulations where all intrinsic conductances of the model were selected from a normal distribution produced results similar to those in which only E_L (analogous to $g_{L(K)}$ in the simulations) and g_{NaP} were heterogeneous, as well as g_{syn}.

3.5 Summary

We have presented a minimalist biophysical model of an oscillatory bursting of respiratory neuron in the mammalian pre-Bötzinger complex [3] and implemented it in the NEURON environment. Furthermore, by coupling these neurons via excitatory AMPA synapses, we

form a hybrid pacemaker network that is suggested to comprise the origin of rhythm generation in vitro. By using an inverse relationship between synaptic strength and connectivity, we have developed a probabilistic method for changing the degree of sparsity of a network without affecting the network dynamics. External drive from a background population can be simulated by a variety of different methods that allow the adjustment of shape, correlation, periodic regularity and mean-level of the signal. The burster can be thought of as oscillators with non-uniform parameters because intrinsic and synaptic heterogeneity have also been introduced to certain parameters. These mechanisms give our model a framework with which one can create a network simulation that more faithfully reproduces the variability seen in experimental recordings.

CHAPTER IV

PRELIMINARY STUDIES OF PROPOSED MECHANISMS TO CREATE RHYTHMIC VARIABILITY

4.1 Effect of Excitatory Background Synaptic Input on Rhythmic Variability

4.1.1 Waveform

In order to discover the possible characteristics of the background population of tonically firing cells, the model was simulated with five different types of excitatory synaptic drive (Figure 11).

1. Constant-level - All cells receive a constant input equivalent to the mean-level of the spiking inputs (Figure 12 A).

2. Individual Periodic - Each cell receives periodic spiking input with the same regular period, while phase is randomly assigned from a uniform distribution (Figure 12 B).

3. Individual Poisson-distributed - Each cell receives spiking input from a poisson process, while phase is randomly assigned from a uniform distribution (Figure 12 C).

4. Global Periodic - All cells receive periodic spiking input with the same regular period (Figure 12 B).

5. Global Poisson-distributed - All cells receive spiking input from a single poisson process (Figure 12 C).

The weight of the background synapse was adjusted so that the excitatory stimulation of the constant-level input would be equivalent to the four spiking inputs at a fixed frequency as seen by the AMPA synapse located on the burster neuron. For each simulation, the transients were allowed to decay for 60 seconds and then data was recorded for 60 seconds. Since only 60 seconds of simulation time were recorded we decided that any simulations

Figure 12: Time series plots of excitatory background input effect on AMPA synapse (no synaptic input from other burster neurons) (A) Constant-level (B) Periodic (C) Poisson-distributed

which showed two or fewer bursts (i.e. burst period less than 20 seconds) would not be considered since they contain insufficient data in order to calculate the CV of burst period. With respect to the biological system we are modeling, discarding these simulations is acceptable since recordings of the pre-Bötzinger complex begin bursting at a frequency of ~ 0.05 Hz, which corresponds to a maximum burst period of 20 seconds. Nineteen random distribution of parameters were used and simulations were run from each of the five different types of excitatory drive. Therefore, for each parameter set the only independent variable was the type of background input. The constant-level type of input sets a baseline minimum amount of variance due solely to heterogeneity of the intrinsic parameter g_{NaP}, but not $g_{L(K)}$ and inter-burster synapses g_{syn}(Figure 12 A). This allowed us to perform a t-test to determine whether the characterization results from the four types of spiking excitatory background input were statistically different from the constant-level input (Table 4). The mean and standard error bars are plotted in Figure 13. Analogous results were obtained for simulations were $g_{L(K)}$ was also heterogenious. However, the CV for these simulations were proportionally higher and had greater variability between trials. The burst periods for these simulations were also uniformly less than the homogenious trials. Though the steady-state values of all three waveforms in Figure 12 are equivalent at the output of the

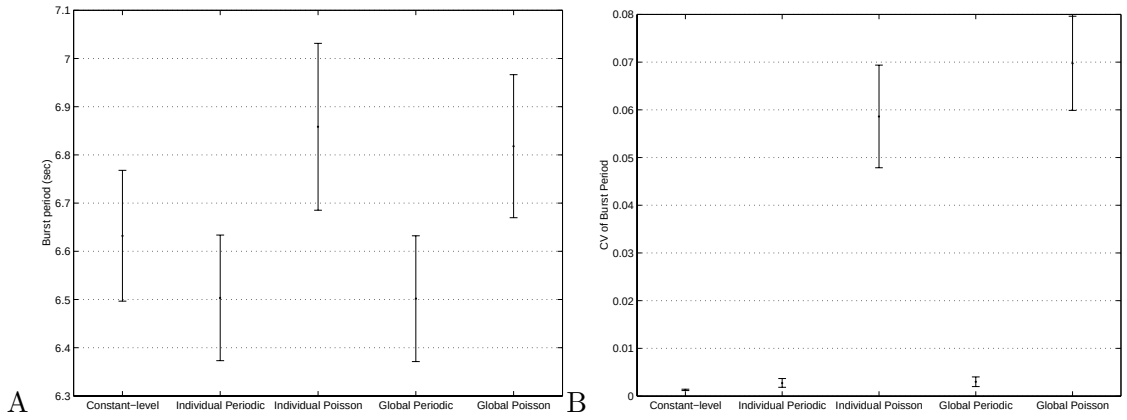

Figure 13: Characterization results with standard error of simulations different types of background input for E_K = -83 mV (n = 19)(A) Burst period (B) CV of Burst period

Type	Average synaptic input level (nS)
Constant-level	.2484
Individual Periodic	.2527
Individual Poisson-distributed	.2378
Global Periodic	.2527
Global Poisson-distributed	.2381

Table 3: Total of synaptic input for burster cells in network (n = 2, $g_{background}$ = .15 nS)

spike generator, when the mean-level of AMPA (synaptic input) conductance was measured in networks with identical intrinsic and synaptic properties differences were found (Table 3). The network was configured with an all to all connection and had heterogenous distribution of g_{NaP} and g_{syn}. The lengthening in burst period by the poisson-distributed spiking models can be accounted for by saturation of the AMPA synapses. While during times when many events are received by the synapse, g_{syn} rises above the mean-level conductance and saturates. Additional inputs can only extend the length of transmitter release. However, during times of infrequent events the g_{syn} drops below mean-level conductance. The overall effect is to reduce the effective input conductance to the slice. These models also produce the most variance in synaptic conductance, due to the same effects (Figure 12). It can be shown that the mean CV of burst period over the nineteen simulations is statistically different from the mean-level case for the poisson-distributed background inputs (Table 4). This is an interesting result because the variability of the input processes are on the timescale of milliseconds, while the variance of burst period is on the order of seconds.

While the differences for the simulations with poisson-distributed types of input can be primarily attributed to synaptic saturation, the decreased burst period in simulations with the periodic types of input must be due to emergent network properties.

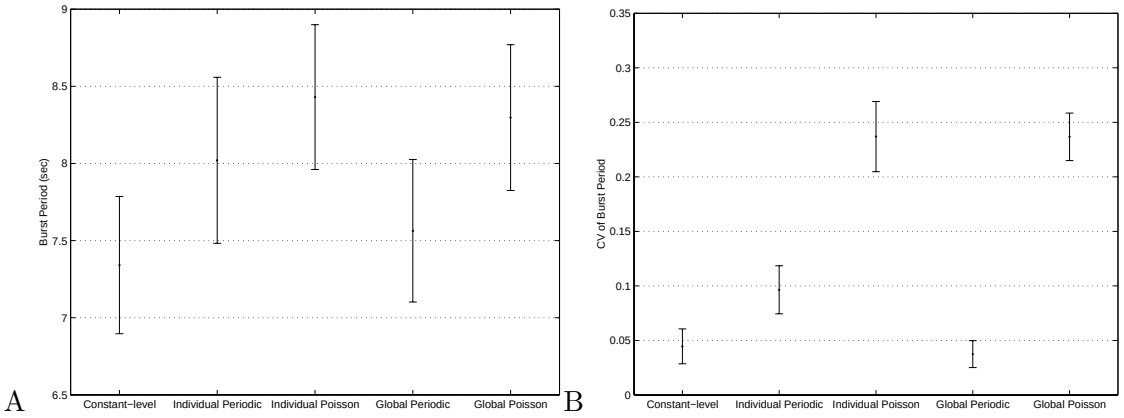

Figure 14: Characterization results with standard error of simulations different types of background input on a network of Model I neurons cells [3] for E_L = -65 mV (n = 19)(A) Burst period (B) CV of Burst period

One plausible mechanism would be that the synchronized spikes (global periodic spiking) depolarize the slice more effectively. In a different set of simulations of models with a single leak channel, E_L that was heterogeneously distributed and had a lower baseline level of membrane depolarization (Figure 14), simulations with global periodic excitatory background input had a burst period much lower than the other spiking methods and very close to then constant-level input. Two interesting findings can be taken from these simulations, in simulations with homogenous sodium and postassium leak channels and a higher baseline level of depolarization, simulations with periodic inputs are stimulated by this input more effectively than a constant-level input. The other finding is that heterogeneity appears to make the phase differences in a periodic input reduce the depolarizing effect of the input as seen by the transverse slice.

4.1.2 Mean level of excitatory background input

The first parameter tested was the mean-level of conductance which controls the amount of excitatory background input received by the slice. The individual poisson-distributed

Type	p-value CV test	p-value BP test
Individual Periodic	.18369	0.00000
Individual Poisson-distributed	.00019	0.15686
Global Periodic	.15500	0.00000
Global Poisson-distributed	.00001	0.09216

Table 4: Hypothesis Tests that CV & BP have the Same mean as Constant-level excitatory background synaptic input (n = 19)

spiking input was chosen because it showed a high degree of variance relative to constant-level input. Similiar results are obtained for individual periodic spiking input. E_K is set to -83 mV, because around this value the simulation produces bursting output. Since the precise amount of input received by the slice is unknown, the value of $g_{background}$ was swept from 0 to .5 nS. The CV of burst period decreases with increased background input

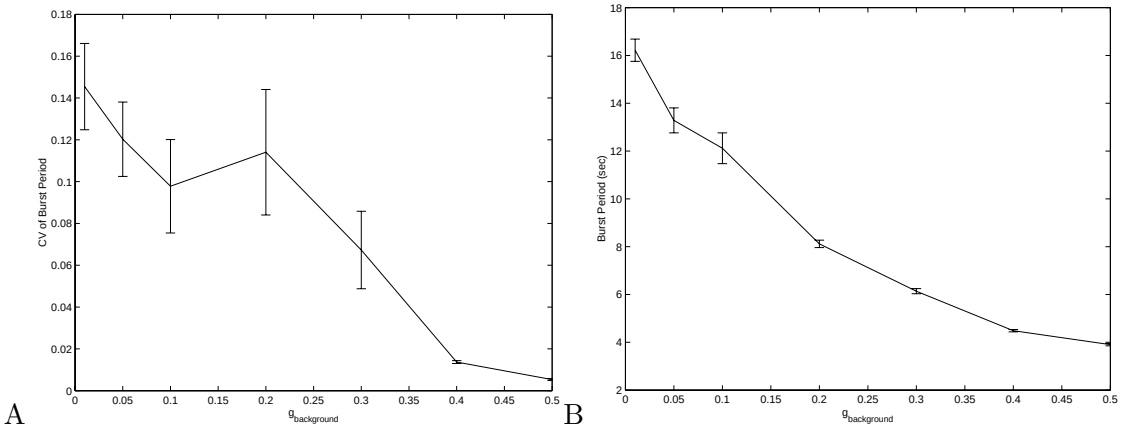

Figure 15: Variation of characterization results as a function of mean level of independent poisson-distributed background input (A)CV of burst period (B)Burst period (n = 5, E_K = -83 mV

(Figure 15 A). This is because as the greater excitatory background input depolarizes the the transverse slice and puts more cells into the bursting and beating regime. As more cells are active, the effect of the heterogenoity gets blended away [6] and the slice output is more uniform. As expected the burst period decreases with increased background input (Figure 15 B). This depolarization effect explains why similar effects are observed regardless of the background input type.

4.1.3 Correlation of background input

In the model, the degree of correlation of the background input can be varied. This is accomplished by creating one background input source for each individual cell and then one global background input source. The degree of correlation of background input can be controlled by weighting the amount of background input signal coming from the individual source versus the global source. The individual background inputs are designed to be independent of each other and the global source, since they each represent a unique poisson process with a uniformly distributed start time. The probability of correlation and probability of connection were both stepped from .1 to 1 see if uncorrelated input (independent poisson-distributed) had more of an effect in a sparsely connected network. Each correlation-connection set was run on the same five randomly distributed intrinsic parameter sets at E_K at -83 mV and $g_{background}$ of .3 nS. The CV and burst period are nearly independent of correlation regardless of the value of connectivity (p). The result of an all-to-all (p=1) connected network shown in Figure 16 can be considered representative of all simulation sets.

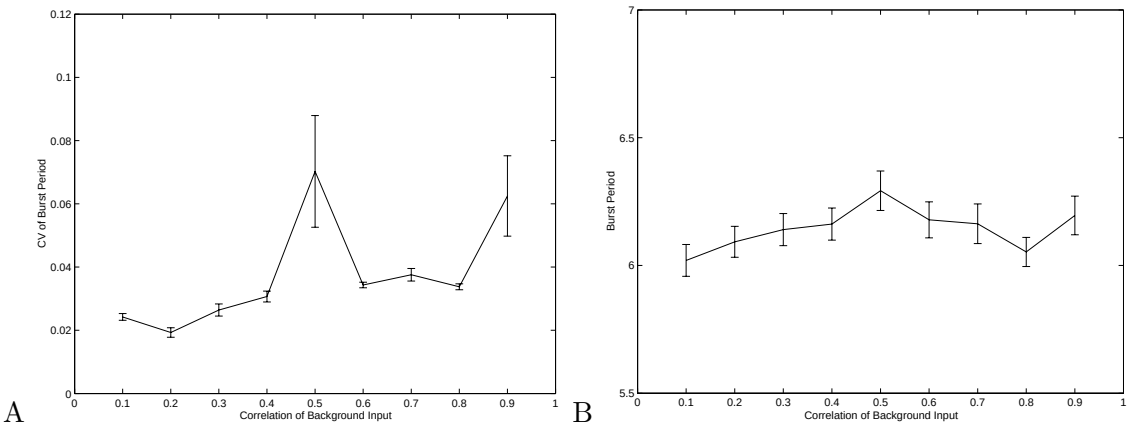

Figure 16: Variation of characterization results as a function of correlation of poisson-distributed background input at $E_K = -83$ mV (n = 5)(A)CV of burst period (B)Burst period

The spike around correlation is indicative of the characterization's algorithm failure to detect a single spike in one simulation as both CV and BP just at the same place. Confirmation of this occurance was verified by observation of the simulated data set and

characterization results.

4.2 Effect of connectivity of the network on rhythmic variability

In previous experimental work [9], the transverse slice was bisected experimentally to explore the effects of excitatory synaptic coupling on burst period and stability of the population activity. These experiments show that the weakened synaptic coupling is insufficient to completely synchronize the pacemaker cells and thus the pre-Bötzinger complex normally developed cycle-to-cycle variability. The cycle-to-cycle fluctuations can be attributed to reductions in coupling strengths.

In the simulations, the coupling and connectivity of the network can be controlled by varying the probability of the existence of a connection between any two cells. A cell cannot be connected to itself. In order to maintain the same mean amount of synaptic input into each cell, the strength of the synaptic connection is inversely proportional to the probability of a connection. This was done because it has been shown (Figure 15) that increasing the amount of synaptic input alter the firing characteristics (i.e. decrease burst period). However, we want to observe the potential mechanisms for producing variability, so it is important to maintain a constant level of synaptic input within the pre-Bötzinger complex while varying the degree of connectivity.

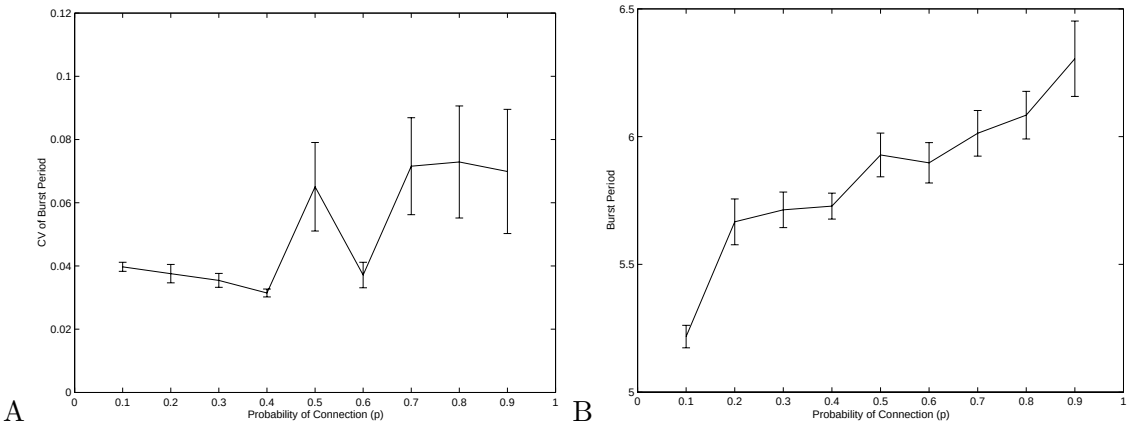

Figure 17: Variation of characterization results as a function of connectivity at E_K = -83 mV (n = 5) (A)CV of burst period (B)Burst period

The probability of connection was stepped from .1 to 1 see if uncorrelated input (independent poisson-distributed spiking) had more of an effect in a sparsely connected network. However, we did not find that evidence of any effect. Correlation of the background excitatory input was then stepped from being total uncorrelated (independent poisson-distributed spiking) to being completely correlated (global poisson-distributed spiking). As expected from the previous section correlation did not have a significant effect on the results and the results obtained from the simulations with independent poisson-distributed spiking excitatory background input can be consider representative of all degrees of correlation. Each probability of connection-correlation set was run on the same five randomly distributed intrinsic parameter sets at E_K at -83 mV and $g_{background}$ of .3 nS.

The results of the characterization algorithm from simulations with independent poisson-distributed spiking excitatory background input show that burst period increases with probability of connection (Figure 17 B). This is a much different phenonoem than previous studies [4] where a mean-level of input caused CV to decrease with increasing probability of connection, while BP stayed relatively constant. Considering that synaptic strength varies inversely with probability of connection, this could be analogous to what happens in Section 4.1 in the global periodic spiking simulations. In both instances, the slice taken as a whole is hit with fewer but more powerful inputs and this decreases the burst period relative to a more temporally spread input. The effect on CV of burst period is very minimal. The slightly increased values of CV at higher p values is also accompanied by much larger standard error bars indicating that the CV varied much more between each simulation. This could very well be a sampling effect as the number of bursts per simulations would decrease as burst period increases.

4.3 Effect of parameter heterogenity of individual bursters on rhythmic variability

To test the effect of heterogeneity on the variability of synchronous bursting, simulations were performed in which the amount of variability of the leakage conductance was varied. This is preferable to varying E_K to affect baseline membrane depolarization level since it can

be presumed that the extracellular concentration of K^+ is relatively constant throughout the slice. Cells with intrinsic behavior that diverges from the rest of the network become more influential on the network rhythm in a smaller sized population.

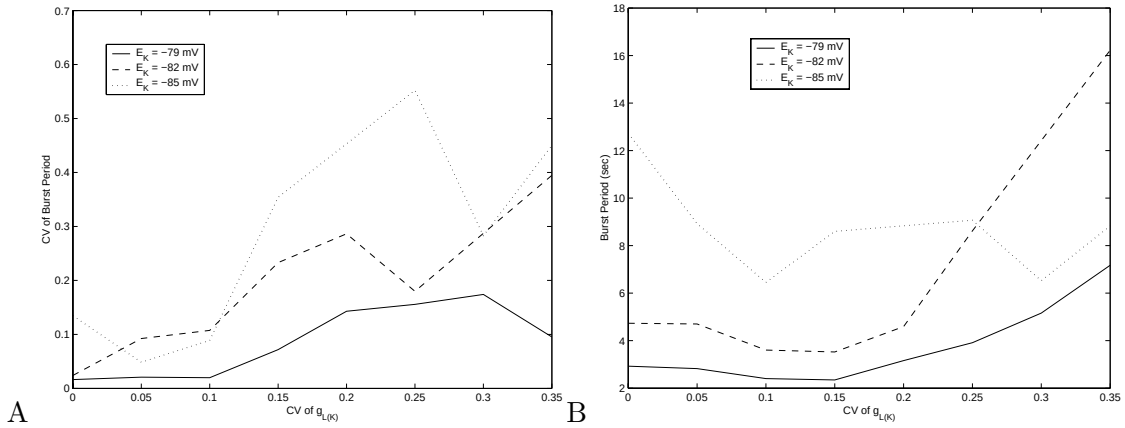

Figure 18: Effects of heterogenous membrane depolarization of burster cells by changing variability of $g_{L(K)}$ on characterization results (Single parameter set, n=1) (A) CV of burst period (B) Burst period

One notes from Figure 18 that the CV of burst period increases as the variability of the potassium leakage conductance increases for the lower values of E_K. This is caused because the slice is has a lower baseline level of membrane depolarization and fewer cells are active and thus those that are active play a greater role in generation of the rhythm and differences between these cells are strongly exhibited.

4.4 Summary

Our preliminary studies found that background input in the form of a poisson process could produce statistically significant levels of variance. This is interesting because the input processes are on the timescale of milliseconds, while the variance appears on the order of seconds. We established an inverse relation between the variance and the mean level of input and was able to dismiss the effect of correlation of input on the variance. An interesting effect was noted both in the application of global periodic spiking input and then similarly in the case of sparsely connected networks. It seems that the burst period is more affected by fewer large synaptic inputs than the same overall amount of input spread over a larger number of synaptic events. Finally, we noted that varying the heterogeneity

of the leakage current could produce fairly sizable proportional effect of the CV of burst period.

CHAPTER V

CHARACTERIZATION OF EXPERIMENTAL DATA

In order to test our simulations ability to recreate rhythmic variability, we needed to characterize experimentally obtained data sets.

5.1 Experiment Data Sets

We obtained mammalian respiratory recordings from both mice and rats. The data was collected from suction electrodes recording extracellular population activity from the XII ventral root of a rhythmically active pre-Bötzinger slice. Data was collected for several different experiments. Each experiment consists of a series of recordings over range of K^+ concentration in the extracellular bathing medium in order to control baseline excitability of the slice. The first data set, refered to as the NIH data set, was collected from rats over a range of extracellular K^+ concentration from 5 to 18 mM over as many as ten experiments. The second data set, refered to as the UCLA data set, was collected from mice over a range of extracellular K^+ concentration from 3 to 12 mM over two experiments.

The novel approach of characterizing rhythmic variability described in chapter two was used to characterize experiment data in order to find experimental values of CV. Standard error bars are included in the graphs.

For the NIH data set, as expected the burst period (Figure 19 A) decreases as the concentration of K^+ increases over the part of the K^+ concentration range that clearly exhibits bursting (i.e. 8-13 mM), since increased concentration depolarizes the slice causing it to be more active. Rhythmic variability as characterized by CV of burst period (Figure 19 B) roughly increases with increasing K^+ concentration with a notable peak around 11 mM. The slice transitions from clearly defined bursting to beating behavior at high concentration of extracellular potassium, and thus the characterization results are not meaningful.

For the UCLA data set, as expected the burst period (Figure 20 B) decreases as the

concentration of K^+ increases disregarding the very low K^+ concentration where bursting is not clearly exhibited (i.e. 3-5 mM). Like in the NIH data, rhythmic variability as characterized by CV (Figure 20 A) roughly increases with increasing K^+ concentration with a notable peak around 7 mM.

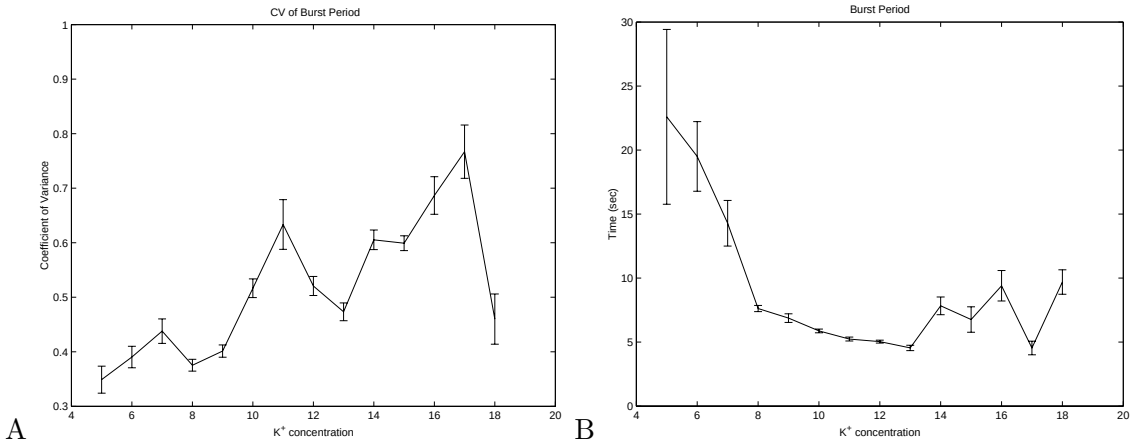

Figure 19: Variation of characterization results as a function of K^+ concentration (NIH Data) (A) CV of Burst period (B) Burst period

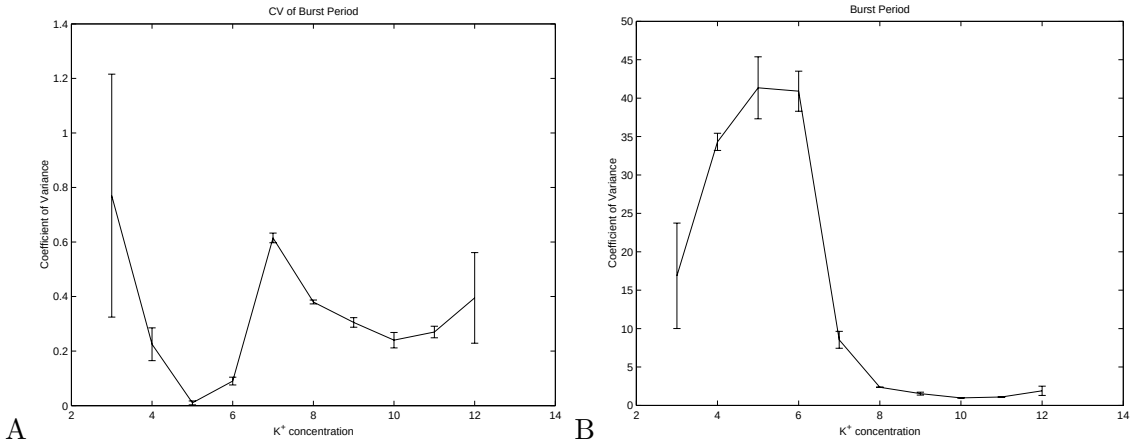

Figure 20: Variation of characterization results as a function of K^+ concentration (UCLA Data) (A) CV of Burst period (B) Burst period

5.2 Simulating effects of extracellular K^+ concentration

Prior work testing the model with experimental preparations [9] have shown that the real and model neurons commenced bursting with a frequency of approximately $\sim$0.05 Hz at low extracellular K^+ concentration corresponding to low values of E_K and exhibited maximum

burst frequency of $\sim$ 0.9 Hz at high extracellular K^+ concentration and values of E_K. However, changes in extracellular K^+ concentration cannot be directly equated to E_K in the model due to non-Nerstain behavior [15]. Despite not knowing the exact relationship, we do know that increasing extracellular K^+ concentration depolarizes pre-Bötzinger complex cells and also the cells that provide the excitatory background input. Due to the positive relationship between E_K and excitatory background input, we decided to run a series of simulations in which both were varied in order to produce a matrix of CV and BP. The thought is by placing a trajectory increasing in both E_K and $g_{background}$ one could then map experimental extracellular K^+ concentrations to E_K levels in the model. Once this work was completed, one could then analyze how well the model predicted changes of CV and BP caused by varying extracellular K^+ concentration.

We chose to use the independent poisson-distributed model with the burster cells connected all to all. This model was chosen because it produced the highest level of CV and is biologically plausible. $g_{background}$ was swept from .01 to .5 nS. E_K was varied from -85 to -78 in .5 mV steps. Each E_K-$g_background$ pair was tested on five randomly distributed intrinsic parameter sets. The simulations were run for 60 seconds to allow transients to decay and then the data was recorded for 60 seconds. Simulations with burst periods less than 20 seconds were discarded as previously mentioned (note the white squares on Figure 21). Therefore, if the model were to accurately follow the experimental data (Figures 19 & 20), the burst period should decrease as E_K increases.

5.3 Comparison of Simulation Results to Experimental Data

This result is confirmed in Figure 21 A. Disregarding the very low concentration K^+ data in the UCLA data, the experimental CV has an overall increasing trend with extracellular K^+ concentration, with a spike within the bursting regime. This spike is at a different concentration for the mice and rat data. Further complicating analysis of the CV results is that the relation between extracellular K^+ concentration is non-linear over the physiological range [15]. It has been shown that membrane potential, which controls frequency of the slice is relatively insensitive to K^+ in this range. With these considerations in mind, it is

not possible to define trajectory increasing E_K and $g_{background}$ that is consistent between Figure 21 A & B. and with the experimental data in Figures 19 & 20.

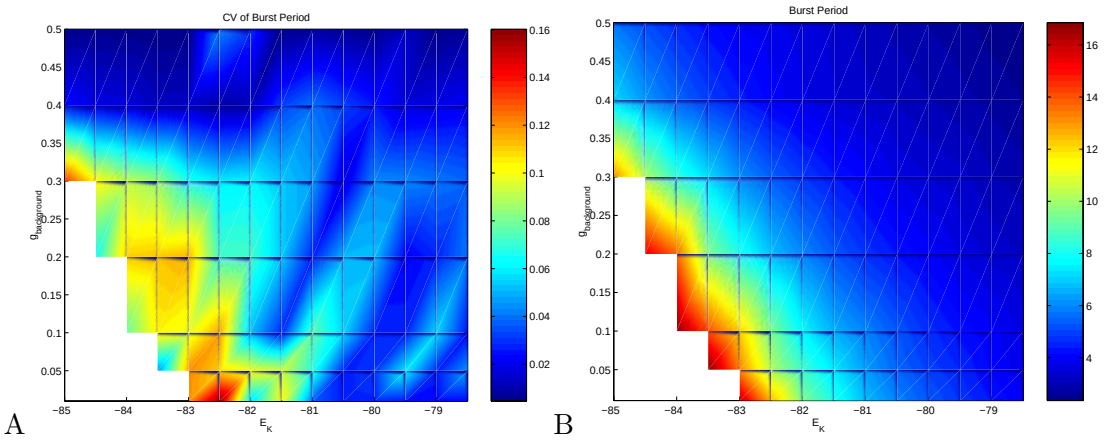

Figure 21: Variation of characterization results as a function of E_K+ and $g_{background}$ (n = 5) (A) CV of Burst period (B) Burst period

Using the poisson-distributed excitatory background input has been shown produce statistically significant increases in the level of cycle-to-cycle variance (See Table 4). However, even with this increase, the model does not approach the levels of variance found in experimental data sets. The limitations of our model are straightforward. A minimalist model while computationally efficient cannot account for intricate and potentially very complex phenomena by its very nature.

CHAPTER VI

COMPUTATIONAL PERFORMANCE OF MORE EFFICIENT NEURON MODEL IN A NETWORK SETTING

The plethora of simulations required to perform this study required a large amount of computational power. A more efficient model that could greatly reduce the computational time to run a simulation would allow the experiementer freedom to run a greater breathe of simulation configurations. Simulation, analysis and prediction are much easier with models that are computationally simpler.

6.1 Hybrid Integrate-and-Fire Model

The model incorporates Hodgkin-Huxley style equations to evolve the subthreshold currents and includes integrate and fire mechanisms to characterize spike events and mediate interactions between subthreshold and spiking currents [2]. This reduction of a Hodgkin-Huxley (HH)-style bursting model to a hybridized integrate-and-fire (IF) formalism is based on a thorough bifurcation analysis of the neuron's dynamics. The hybrid IF model successfully reproduces the dynamic behavior and temporal characteristics of the full model over a wide range of activity including bursting and tonic firing. Comparisons of timed computer simulations of the reduced model and the original model for both single neurons and moderately-sized networks ($n \leq 500$) show that this model offers improvement in computational speed over the HH-style bursting model (Figure 22). Endogenously bursting neurons have been the subject of intensive mathematical modeling and computer simulation. Due to the rich repertoire of biophysical mechanisms involved in bursting, mathematical models which attempt to accurately reproduce these dynamics can be complex. Even the simplest reduced bursting models [3] must still include variables that evolve on two radically different

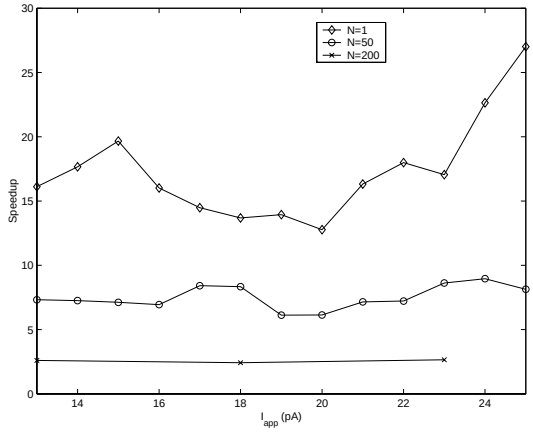

Figure 22: Computation performance of hybrid vs. full model over a range of I_{app} corresponding to slow bursting, fast bursting and tonic spiking

time scales, typically three to four orders of magnitude. The slow variables govern a slow oscillation in the membrane voltage that alternates between a silent state and an oscillatory state. The oscillatory state is characterized by the firing of action potentials governed by fast variables, and the periodic alternation between silence and spiking is referred to as bursting.

Computationally simpler models lend themselves more readily to simulation, analysis and prediction. In general, efforts at simplification focus on reducing the complexity of bursting systems while maintaining a relationship between the model and experimentally measured quantities. Usually the system is separated into two subsystems which characterize the fast and slow dynamics of the neuron. One of the simplest computational model neurons is the integrate-and-fire (IF). In the IF model [23], spike frequency and voltage baseline are controlled by a rule that dictates the resetting voltage, V_{Reset}, after the threshold voltage, V_{Thresh}, is crossed. This model captures certain fundamental features of the neuron such as the evolution of a subthreshold membrane voltage, the generation of a 'spike event' when a given voltage threshold is crossed, and the return of membrane voltage to a baseline after the spike event. Adaptations of either V_{Thresh} and V_{Reset} have been shown to produce more complex behavior. More elaborate variants of IF models have incorporated the effects of HH-style conductances by approximating the voltage-dependent rate constants and deriving piecewise analytic expressions for the gating variables [11].

For our hybrid integrate and fire model, we derive functions for V_{Thresh} and V_{Reset} in terms of the single slow variable h from features of the bifurcation diagram of the reduced fast subsystem. In addition, we use the bifurcation analysis to quantify the perturbational effects of the action potential on the slow variable. The net result is a Hodgkin-Huxley-like formalism for the subthreshold currents and an IF formalism for the spiking currents, with the interactions between them fully described.

$$C\frac{dV}{dt} = -I_{NaP-h}(V) - I_{Leak} + I_{app} \tag{16}$$

$$\frac{dh}{dt} = \frac{h_\infty(V) - h}{\tau_h(V)} \tag{17}$$

When $V \geq V_{Thresh}(h), V = V_{Reset}(h) h = h + \Delta h(h)$

This model displays dynamic behavior and temporal characteristics of the full HH style model over a wide range of activity including bursting, beating and spiking, but offers significant improvement in computation speed over the full model. Comparisons of timed computer simulations of the reduced model and the original model for moderately-sized networks ($n < 500$) across a range of applied current, $13 \leq I_{app} \leq 25$ pA show that this model offers improvement in computational speed over the HH-style bursting model. The parameter I_{app} was chosen since it biases the mode of cellular activity. All timing runs were of equal length and given initial conditions already on the stable limit cycle. Simulation times were obtained using UNIX operating system calls that provide a measure of true CPU time of the running process. All file output was disabled so that the timing results were not contaminated by disk-writing overhead.

For network simulations, we implemented an excitatory network model [4] that consists of heterogeneous neurons all-to-all connected by excitatory AMPA synapses. We ran simulations consisting of 50-200 neurons and compared the process run time of the reduced model network and the full model network. Timings were made after startup transients had died away and for the network simulating 60 seconds of network activity. As the size of the network increased, the conductance of each synapse was decreased to maintain networks with similar mean levels of overall synaptic input per cell and similar overall dynamics

n	p = 1	p = .1
50	7.645	7.957
200	3.259	3.197
500	1.858	2.844
1000	1.282	1.344

Table 5: Computation performance of hybrid vs. full model (speedup) at different probability of connection

independent of n.

6.2 Speedup Calculation

Comparisons were done for three values of I_{app} corresponding to three different modes of activity: slow bursting, fast bursting and tonic spiking. Varying I_{app} in the network simulations is algebraically analogous to varying the leakage reversal potential E_L [4].

We investigated to what extent the use of our reduced model was responsible for this reduction in speedup. While the reduced model is clearly simpler, the added complexity of finding the times of crossings of V_{thresh} may not simply scale linearly with the size of the network for a network simulation. Even though NEURON uses local time steps for each cell, another potential cause for the reduction of speedup is the larger number of synaptic events that NEURON must process for larger and larger networks. To address these issues, we ran simulations for the full and reduced model, for both p=1 and p=0.1, and for n = 50, 200, 500, and 1000; where n is the number of neurons in the network and p is the probability of a connection (Table 5). When $p = 0.1$, the conductance of each synapse was increased by $1/p$ to maintain similar network dynamics for comparable benchmarking.

To analyze this performance data, we made the following assumptions:

1. There is a fixed cost for processing a synaptic event, and the amount of time devoted to solving synaptic events scales with $pn(n-1)$;

2. The time spent numerically integrating the intrinsic cell models scales with $O(n^x)$, where $x \geq 1$. This is based on numerical linear algebra assumptions. The computational complexity of solving a set of m differential equations is of $O(m^2)$, but can be as low as $O(m)$ if all the equations are independent of one another. The independence

Model	K_i (sec)	x (unitless)	K_s (sec)
REDUCED	0.0902	1.8577	0.0097
FULL	7.614	1.2669	0.0122

Table 6: Simplex parameter fits of how computational time scales with network size

of individual cell models and the "local dt" option in NEURON may make the computation time scale with $O(n)$. Conversely, larger numbers of synaptic inputs create more events and thus more time-steps to be solved per cell, and both the number of synaptic events as well as a worst case numerical integrator scales with $O(n^2)$.

If $x < 2$ and n becomes arbitrarily large, we would expect the computation time to scale with n^2. If this were to occur, it suggests that for large n the overhead in processing synaptic events is the dominant effect on computation time. A plot of computation time vs. n on a log-log scale (not shown) reveals a slope of approximately 2 for the reduced model and about 1.5 for the full model. If we assume that the reduced model is of less computational complexity than the full model, this results suggests that the overhead associated with processing synaptic events is responsible for the reduced speedup for large n.

To further investigate this issue, we used the Nelder-Meld simplex method to identify parameters for the following formulation, choosing parameters that minimize the log error between the formula and the data points, with an additional constraint that $x \geq 1$:

$$T(n) = K_i n^x + K_s pn(n-1) \tag{18}$$

where K_i represents the computational overhead for solving the dynamic equations for a single cell and K_s represents the computational overhead for handing a single synaptic event. Our best-fit results are tabulated in Table 6.

While we did not impose such a constraint, we would expect that the K_s values would be similar for the full and reduced model, since NEURON processes both identically. In practice, the estimated parameters were within 25% of each other. The estimate also suggests that K_i is much less for the reduced model, which is to be expected due to its lower computational complexity for a single cell. Finally, it shows that x is about 1.86 for

the reduced model and 1.27 for the full model. From these estimates we conclude that:

1. While the reduced model is much faster for a single cell speedup results and lower K_i, for a network its computational complexity scales greater with n than the full model, somewhat limiting speedup for network simulations; and

2. Since $x < 2$, the overhead processing synaptic events ultimately becomes the limiting factor affecting the computation time of large network simulations.

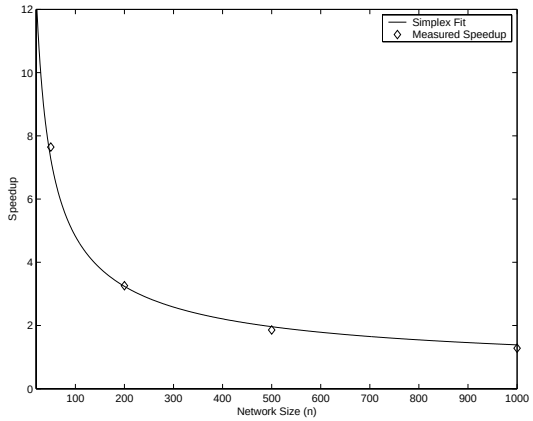

Figure 23: Speed up as a function of network size ($I_{app} = 14$ pA)

We make these conclusions with several caveats. They are merely based on fits to performance timings of a single simulation, and there are many model and simulator-dependent factors and parameters that can affect these results. They were also benchmarked for one particular simulation with a particular mode of activity (network wide bursts separated by periods of silence), which will also affect timing results.

6.3 Summary

We conclude that while the reduced model is much faster than the full model for a single cell, its computational complexity scales more with n than the full model, leading to reduced speedup for larger simulations. Furthermore, the overhead in processing synaptic events for large networks makes the speedup gains for any reduced cell model negligible for n much greater than 1000 (Figure 23). Thus our reduced model formulation is most effective in gaining speedup for networks of $n \leq 500$ in particular, and networks of less than 1000

neurons in general. Despite the potential time savings, all simulations in Chapters 3-5 were done based on the the full model to ensure consistency with legacy data.

CHAPTER VII

CONCLUSIONS

7.1 Summary of Work

We have developed a novel metric for characterizing variability in rhythmic periodicity. We created a computational model that incorporated potential mechanisms for producing rhythmic variability from a deterministic neuron model. It had been known that parameter heterogeneity can produce some of this desired variability. The main thrust of the research was finding types of excitatory synaptic background input that could contribute to this variability. To that end we did find that using a poisson-distributed process to generate spiking events, one can produce a statistically significant level of additional variability. We were able to discount the role of correlation of background input as a significant factor in rhythmic variability. Furthermore, we saw that the burst period is more affected by fewer large synaptic inputs than the same overall amount of input spread over a larger number of synaptic events in two distinct experiments. However, by using the coefficient of variance as a metric, it can be shown that our models do not produce the levels of variability found in experimental data sets. We were unable to successfully map E_K to extracellular potassium concentration, which indicates that our model may lack some necessary complexity.

In the pursuits of the goals of this research, we decided to use very minimalist models for multiple reasons. Primarily they allow greater understanding of the key underlying processes. However our results confirmed the weakness of this approach. Our models could not account for all the complex behavior of the system we were modeling. A second reason to use a minimal model is computational efficiency. To this end, we present a reduced model which has been shown to produce efficiency gains in the single cell and small to medium size networks. We found that while the reduced model is much faster than the full model for a single cell, speedup for larger simulations such as over 1000 is much reduced. This is because its computational complexity scales more with n than the full model.

7.2 Future Work

One unexpected finding was the decrease of burst period when stimulated with large periodic spikes, as evidenced by the connectivity results. Likewise, the periodic spiking background input seemed to depolarize the slice to a greater effect. It is possible that these may be related effects. Further study need to be conducted to understand these emergent network property and its causes.

Currently, the models do not produce the level of variance found in experimental data. One interesting experiment would be to incorporate ion-channel noise into the existing model as that would be a most likely and known source of variability. Though we had stated that these channels are computational expensive to model, the computational power is readily available, as are software packages such as MCELL, which can be tied into our NEURON model.

REFERENCES

[1] Bianchi, A. L. and M. Saubie-Denavit, J. C., "Central control of breathing in mammals: neuronal circuitry, membrane properties, and neurotransmitters," *Phys. Rev. Lett.*, vol. 75, pp. 1–45, 1995.

[2] Breen, B. J., Gerken, W. C., and Butera, R. J., "Hybrid integrate-and-fire model of a bursting neuron," *Neural Computation*, vol. To be published, 2003.

[3] Butera, R. J., Rinzel, J., and Smith, J. C., "Models of respiratory rhythm generation in the pre-Bötzinger complex. I. Bursting pacemaker neurons," *J. Neurophysiol*, vol. 82, pp. 382–397, 1999.

[4] Butera, R. J., Rinzel, J., and Smith, J. C., "Models of respiratory rhythm generation in the pre-Bötzinger complex. II. Populations of coupled pacemaker neurons," *J. Neurophysiol*, vol. 82, pp. 398–415, 1999.

[5] De Vries, G. and Sherman, A., "Channel sharing in pancreatic beta-cells revisited: Enhancement of emergent bursting by noise," 2000.

[6] De Vries, G. and Sherman, A., "From spikers to bursters via coupling: Help from hetergeneity," *Bulletin of Mathematical Biology*, vol. 00, pp. 1–21, 2001.

[7] De Vries, G., Sherman, A., and Zhu, H. R., "Diffusively coupled bursters: Effects of cell heterogeneity," *Bulletin of Mathematical Biology*, vol. 60, pp. 1167–1200, 1998.

[8] DeFelice, L. J. and Isaac, A., "Chaotic states in a random world," *J. Stat. Phys*, vol. 70, pp. 339–352, 1992.

[9] Del Negro, C. A., Johnson, S. M., Butera, R. J., and Smith, J. C., "Models of respiratory rhythm generation in the pre-bötzinger complex. III. Experimental tests of model predictions," *J. Neurophysiol*, vol. 86, pp. 59–74, 2001.

[10] Del Negro, C. A., Koshiya, N., Butera, R. J., and Smith, J. C., "Persistent sodium current, membrane properties and bursting behavior of pre-botzinger complex inspiratory neurons in vitro," *J. Neurophysiol*, vol. 88, pp. 2242–2250, 2002.

[11] Destexhe, A., "Conductance-based integrate and fire models," *Neural Computation*, vol. 9, pp. 503–514, 1997.

[12] Destexhe, A., Mainen, Z. F., and Sejnowski, T. J., "An effecient method for computing synaptic conductances based on a kinetic model of receptor binding," *Neural Computation*, vol. 6, pp. 10–14, 1994.

[13] Destexhe, A., Mainen, Z. F., and Sejnowski, T. J., "Synthesis of models for excitable membranes, synaptic transmission and neuromodulation using a common kinetic formalism," *Journal of Computational Neuroscience*, vol. 1, pp. 195–230, 1994.

[14] Feldman, J. L. and Smith, J. C., "Cellular mechanisms underlying modulation of breathing patterns in mammals," *Ann. NY Acad. Sci*, vol. 563, pp. 114–130, 1989.

[15] Forsythe, I. D. and Redman, S. J., "The dependence of motoneurone membrane potential on extracellular ion concentratios studied in rat spinal cord," *Journal of Physiology*, vol. 404, pp. 83–99, 1988.

[16] Funk, G. D., Smith, J. C., and Feldman, J. L., "Generation and transmission of respiratory oscillations in medullary slices: role of excitatory amino acids," *J. Neurophysiol*, vol. 70, pp. 1497–1515, 1993.

[17] Gray, P. A., Janczewski, W. A., Mellen, N., McCrimmon, D. R., and Feldman, J. L., "Modulation of respiratory frequency by peptidergic input to rhythmogenic neurons in the pre-bötzinger complex," *Science*, vol. 286, pp. 1566–1568, 1999.

[18] Hines, M., "A program for simulation of nerve equations," in *Neural Systems: Analysis and Modeling* (Eeckman, F. H., ed.), pp. 127–136, Boston, MA: Kluwer Academic Publishers, 1993.

[19] Hodgkin, A. L. and Huxley, A. F., "A quantitative description of membrane current and its application to conduction and excitation in nevre," *J. Physiol. (London)*, vol. 117, pp. 500–544, 1952.

[20] Johnson, S. M., Smith, J. C., and Feldman, J. L., "Pacemaker behavior of respiratory neurons in medullary slices from neonatal rat," *J. Neurophysiol*, vol. 72, pp. 2598–2608, 1994.

[21] Koshiya, N. and Guyenet, P. G., "Nts neurons with carotid chemoreceptor inputs arborize in the rostral ventrolateral medulla," *Am. J. Physiol.*, vol. 270, pp. 1273–1278, 1996.

[22] Koshiya, N. and Smith, J. C., "Neuronal pacemaker for breathing visualized in vitro," *Nature*, vol. 400, pp. 360–363, 1999.

[23] Lapicque, L., "Recherches quantitatives sur l'excitation electrique des nerfs traitee comme une polarization," *Journal of Physiology (Paris)*, vol. 9, pp. 620–635, 1907.

[24] Lecar, H. and Nossal, R., "Theory of threshold fluctuations in nerves i. relationships between electrical noise and fluctuations in axon firing," *Biophys. J.*, vol. 11, pp. 1048–1067, 1971.

[25] Lecar, H. and Nossal, R., "Theory of threshold fluctuations in nerves ii. analysis of various sources of membrane noise," *Biophys. J.*, vol. 11, pp. 1068–1084, 1971.

[26] Muthuswamy, J. and Thakor, N. V., "Spectral analysis methods for neurological signals," *Journal of Neuroscience Methods*, vol. 83, pp. 1–14, 1998.

[27] Orem, J. and Dick, T., "Consistency and signal strength of respiratory neuronal activity," *J. Neurophysiol*, vol. 50, pp. 1098–1107, 1983.

[28] Ramirez, J. M., Quellmalz, U. J. A., Wilken, B., and Richter, D., "The hypoxic response of neurons within the in vitro mammalian respiratory network," *J. Physiol. (London)*, vol. 507, pp. 571–582, 1998.

[29] Ramirez, J. M. and Richter, D. W., "The neuronal mechanisms of respiratory rhythm generation," *Curr. Opin. Neurobiol.*, vol. 6, pp. 817–825, 1996.

[30] Rekling, J. C. and Feldman, J. L., "Pre-bötzinger complex and pacemaker neurons: hypothesized site and kernel for respiratory rhythm generation," *Annu. Rev. Physiol.*, vol. 60, pp. 385–405, 1998.

[31] Rekling, J. C., Shao, X. M., and Feldman, J. L., "Electrical coupling and excitatory synaptic transmission between rhythmogenic respiratory neurons in the pre-Bötzinger complex," *J. Neurosci.*, vol. 113, pp. 1–5, 2000.

[32] Rinzel, J., "Excitation dynamics: insights from simplified membrane models.," *Fed. Proc.*, vol. 44, pp. 2944–2946, 1985.

[33] Rosenburg, J. R., Amjad, A. M., Breeze, P., Brillinger, D. R., and Halliday, D. M., "The fourier approach to the identification of functional coupling between neuronal spike train," *Prog. Biophys. Molec. Biol.*, vol. 53, pp. 1–31, 1989.

[34] Rybak, I. A., Paton, J. F., and Schwaber, J. S., "Modeling neural mechanisms for genesis of respiratory rhythm and pattern. II. Network models of the central respiratory pattern generator," *J. Neurophysiol*, vol. 77, pp. 2007–2026, 1997.

[35] Rybak, I. A., Paton, J. F., and Schwaber, J. S., "Modeling neural mechanisms for genesis of respiratory rhythm and pattern. III. Comparsion of model performance during afferent nerve stimulation," *J. Neurophysiol*, vol. 77, pp. 2027–2039, 1997.

[36] Rybak, I. A., Paton, J. F., and Schwaber, J. S., "Modeling neural mechanisms for genesis of respiratory rhythm and pattern. I. Models of respiratory neurons," *J. Neurophysiol*, vol. 77, pp. 1994–2006, 1997.

[37] Schwarzacher, S. W., Smith, J. C., and Richter, D. W., "Pre-bötzinger complex in the cat," *J. Neurophysiol*, vol. 73, pp. 1452–1461, 1995.

[38] Smith, J. C., "Integration of cellular and network mechanisms in mammalian oscillatory motor circuits: Insight from the respiratory oscillator," in *Neurons, Networks, and Motor Behavior* (Stein, P., Grillner, S., Selverson, A. I., and Stuart, D. G., eds.), pp. 97–104, Cambridge, MA: MIT Press, 1997.

[39] Smith, J. C., Ellenberger, H. H., Ballanyi, K., Ritcher, D. W., and Feldman, J. L., "Pre-bötzinger complex: a brainstem region that may generate respiratory rhythm in mammals," *Science*, vol. 254, pp. 726–729, 1991.

[40] Smith, J. C., Funk, G. D., Johnson, S. M., and Feldman, J. L., "Cellular and synaptic mechanisms generating respiratory rhythm: insights from in vitro and computational studies," in *Ventral Brainstem Mechanisms and Control of Respiration and Blood Pressure* (Trouth, O., Millis, R., Kiwull-Schone, H., and Schlafke, M., eds.), pp. 463–496, New York: Marcel Dekker, 1995.

[41] Steinmetz, P. N., Manwani, A., and Koch, C., "Variability and coding efficiency of noisy neural spike encoders," *BioSystems*, vol. 62, pp. 87–97, 2001.

[42] White, J. A., Klink, R., Alonso, A., and Kay, A. R., "Noise from voltage-gated ion channels may influence neuronal dynamics in the entorhinal cortex," *J. Neurophysiol*, vol. 80, pp. 262–269, 1998.

[43] Xiang, Z., Greenwood, A. C., Kairiss, E. W., and Brown, T. H., "Quantal mechanism of long-term potentiation in hippocampal mossy-fiber synapses," *J. Neurophysiol*, vol. 71, pp. 2552–2556, 1994.